საქართველოს ტექნიკური უნივერსიტეტი

სტუ

GEORGIAN TECHNICAL UNIVERSITY

FORSCHUNGSZENTRUM JŰLICH

Interferometrical Characterization of the Gas-jet Density Profiles above a 100 µm-Nozzle

Master Thesis

by

Giorgi Kukhalashvili

Supervisors: Markus Büscher (FZJ)

Elguja Kutelia (GTU)

Faculty of Informatics and Control Systems

July 2013

The greatest enemy of knowledge is not ignorance,

It is the illusion of knowledge.

Stephen Hawking

Declaration

I hereby declare that I have written this master thesis without any help from others and without the use of documents and aids other than those stated below. I have mentioned all used sources and cited them correctly according to established academic citation rules.

July 22, 2013

Giorgi Kukhalashvili

Acknowledgement

To say frankly this thesis is not only the description of concrete experiments and its results, but to my mind it can be interpreted as one of the smaller components of newly designed bridges, well foundated just recently and which can be proudly passed over by younger generations on the way to the peak of success. This is a science bridge between Georgia and Germany and a lot of effort and energy has been used to build it up from both sides.

When talking about this bridge, it is impossible not to mention two great constructors Prof. Dr. Hans Ströher and Dr. Andro Kacharava who played incredible huge roles just from the generation of the idea until the full implementation. I really want to thank them for every warm and friendly advice that helped me to adapt and feel comfortable in a new and foreign environment. I also want to thank Prof. Dr. Rudolf Maier a lot for his effort to find resources for my arrival and further stay here. Many thanks to my personal supervisor Priv. Doz. Dr. Markus Büscher for his direct and very attentive attitude to me and for giving me a chance to work and study in Europe's one of the most powerful research centers.

Special and heartful thanks to my dear friend and colleague Ilhan Engin for his brotherful talks and his advices he gave me assiduously. I will really never forget this and Ilhan will always stay in my mind as a real etalon of friend. Many thanks to Malkhaz Jabua for diligently supporting and encouraging me during the whole time of my work, also Zara Bagdasarian for helping me to solve many problems or issues, David Mchedlishvili and David Chiladze for their fruitful advices. Thanks to Astrid Holler for her continuous support and for supplying me with a proper literature.

I want to thank Dr. Alexander Nass for his discussions and helpful advices. Dr. Harald Glücker for helping me to find space and resources for my experiment.

Dipl. Ing. Ulrich Giesen supported me very much during the whole experimental works. I am very thankful and could learn very much from him.

Warm hearted thanks to my Georgian supervisor Prof. Elguja Kutelia for inspiring me to work in scientific directions. His open-hearted and extremely friendly attitude and approach helped me to find the right way in my life. I am grateful to him for having a huge influence on the formation of my personality. Many thanks to Dr. Olga Tsurtsumia for her continuous human and scientific support on me.

Finally, I am extremely grateful to all of the people from the German side, who contributed in my work at Forschungszentrum Jülich. I always felt their supportive and very positive attitude. Thanks to all of the Georgians, with whom I lived side by side in Germany. They facilitated me the difficulty of living abroad, far away from my country and relatives. Time spending with them is unforgettable for me.

Abstract

In the frame of this thesis interferometrical characterizations of gas density profiles (produced by a Laval-type nozzle with an inner diameter of 167 μm) were performed.

The nozzle was designed and manufactured based on the results of simulations and experiments by the Laser acceleration group of the Institute for Nuclear Physics (IKP) of the Forschungszentrum Jülich. The results revealed that it was necessary to use a smaller sized nozzle, than during the pre-experiments. The Laval-shaped nozzle has been constructed with a minimal diameter of 167 μm.

The properties (*i.e.* the Spatial density distribution above the nozzle exit) where measured within this thesis with the help of a Mach-Zehnder interferometer. It was constructed, tested and used on an optical table in a temperature stabilized laboratory at the Central Institute of Engineering, Electronics and Instrumentation (ZEA-1 of the FZJ). It should be emphasized that the experiment has been held under the minimal influences of environmental factors, such as vibration from turbo pump. Argon gas at room temperature was used during the experiment and it was supplied with several applied pressures. The valve has been operated in a vacuum chamber.

The results of the experiment have been recorded by a powerful CCD camera with a large sensor and high-speed recording-transmission option, which guaranteed the high quality of the recorded information. The interferometric images were analyzed by the *Mathlab* code, which enabled the processing of huge amounts of information in short time intervals, and of course, which made the whole analysis more comfortable to use. For the analysis the Abel inversion method was used.

Contents

List of Figures

1. Introduction and Motivation

Electron and ion acceleration in relativistic plasmas induced by multi–TW Lasers is a field of highest interest. The hope is that future compact and relatively inexpensive accelerator facilities can be realized by this technique.

Efficient ion acceleration would require that the Laser pulse leaves the jet at the rear side, thereby pushing electron out of the generated plasma which then build up a strong electric field for subsequent ion acceleration.

It is relatively easy to accelerate electrons from a gas target, because they have a small mass and can be easily influenced, while ions, because they are at least 2000 times heavier than electrons, generally remain in the plasma. Ion acceleration requires the existence of secondary electric field in the plasma, induced by a separation of the accelerated electron cloud and the remaining ions, thus the strong secondary electric field is generated by the charge separation that causes their acceleration. [1]

Experiments performed at the Institute for Laser and Plasma Physics (ILPP) of Heinrich-Heine University Düsseldorf by the Jülich Laser group revealed that the nozzle creating an approximately 1.5 mm thick gas jet was not useful: after the Laser pulse hit on the gas jet, no ions could be detected. According to the theoretical calculations the problem is the thickness of the gas jet. Since the Laser pulses were fully absorbed in the gas jet.

Taking them into account, nozzles with a diameter of 100-200 µm have been constructed in order to solve all the existing problems. While the properties of the gas jet above the nozzle can be theoretically predicted only with limited accuracy, it is necessary to measure the gas density profiles. This can be achieved by an interferometrical method, particularly the Mach-Zehnder interferometer. The measurements reveal what kind of particle density distributions are present at different heights above the nozzle as a function of the backing gas pressures. The most important distance is the height which is profitable for the laser propagation. 500 µm is the minimal distance between the optical axis, *i.e.* the Laser propagation direction, and the upper edge of the nozzle. In case of a smaller distance, a damage of the nozzle the Laser is possible and should be avoided. It is important to know the behavior of the gas jet during the several timing intervals (in ms), in order to find the appropriate time interval for the laser propagation, *i.e.* the timing.

2. Theoretical Background

2.1. The Mach-Zehnder Interferometer

The Mach-Zehnder interferometer is one type of interferometers which is useful for studies of fluid flow, combustion, heat transfer, plasmas, and diffusion. It is frequently used in the study of *e.g.* aerodynamics, plasma physics or heat transfer to measure pressure, density and temperature changes in gases. The name of the interferometer is related to the surnames of the two physicists Ludwig Mach and Ludwig Zehnder, who are the founders of this type of interferometer. [2]

The general setup of the Mach-Zehnder interferometer consists of the optical source, two beam splitters, two mirrors and a detector at the end point. These are the main basic components of the interferometer. But due to the specificity of the given experiment, more components have to be added (*e.g.* beam expander system, spatial filter, diaphragms, several lenses, *etc.).*

In the Mach-Zehnder interferometer, beam splitting occurs before passing the probe (*e.g.* in this case it is the gas jet). Thus, the beamlets propagate through different optical devices (*e.g.* lenses) and get a different phase distortion until hitting on the detector. Figure 2.1 illustrates the general build-up of a Mach-Zehnder interferometer.

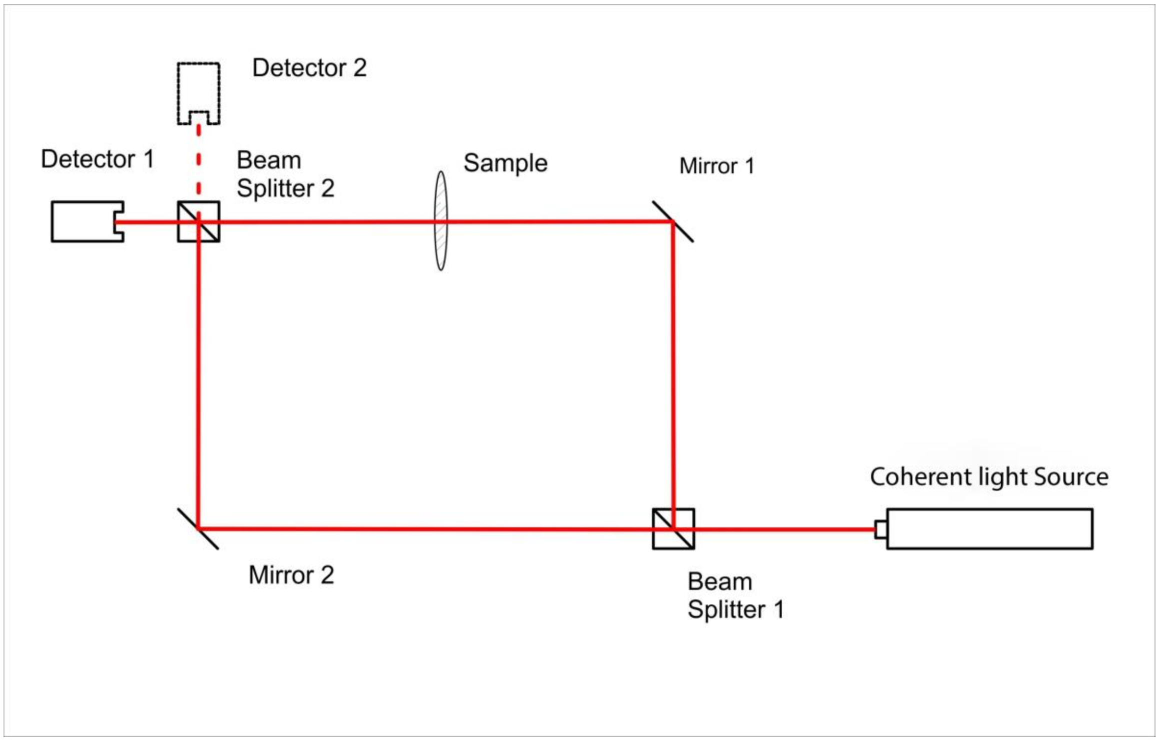

Figure 2.1: The Mach-Zehnder interferometer.

The source creates a beam (*e.g.* a widened HeNe Laser) which is devided with the help of a beam splitter. The two created beamlets propagate in different directions. After the first beam splitter, in the given experiment these directions are perpendicular to each other and afterwards the direction is defined by mirrors. From these two equal beamlets one propagates through the probe inside a sample cell (*e.g.* in the given experiment an argon gas jet created by a µm-nozzle and for the sample cell a vacuum chamber was used), while the other one propagates through air and serves as a reference beam. Both beamlets are recombined with a second beam splitter and superpose. After the superposition of the two beams, horizontal interference fringes can be observed on the detector (*e.g.* In this case it is a CCD camera). Before the picture is detected with the CCD, it is enlarged with an aspherical lens. As it said above, finally an interference pattern is formed and fringes can be detected (*cf.* Fig. 2.2.)

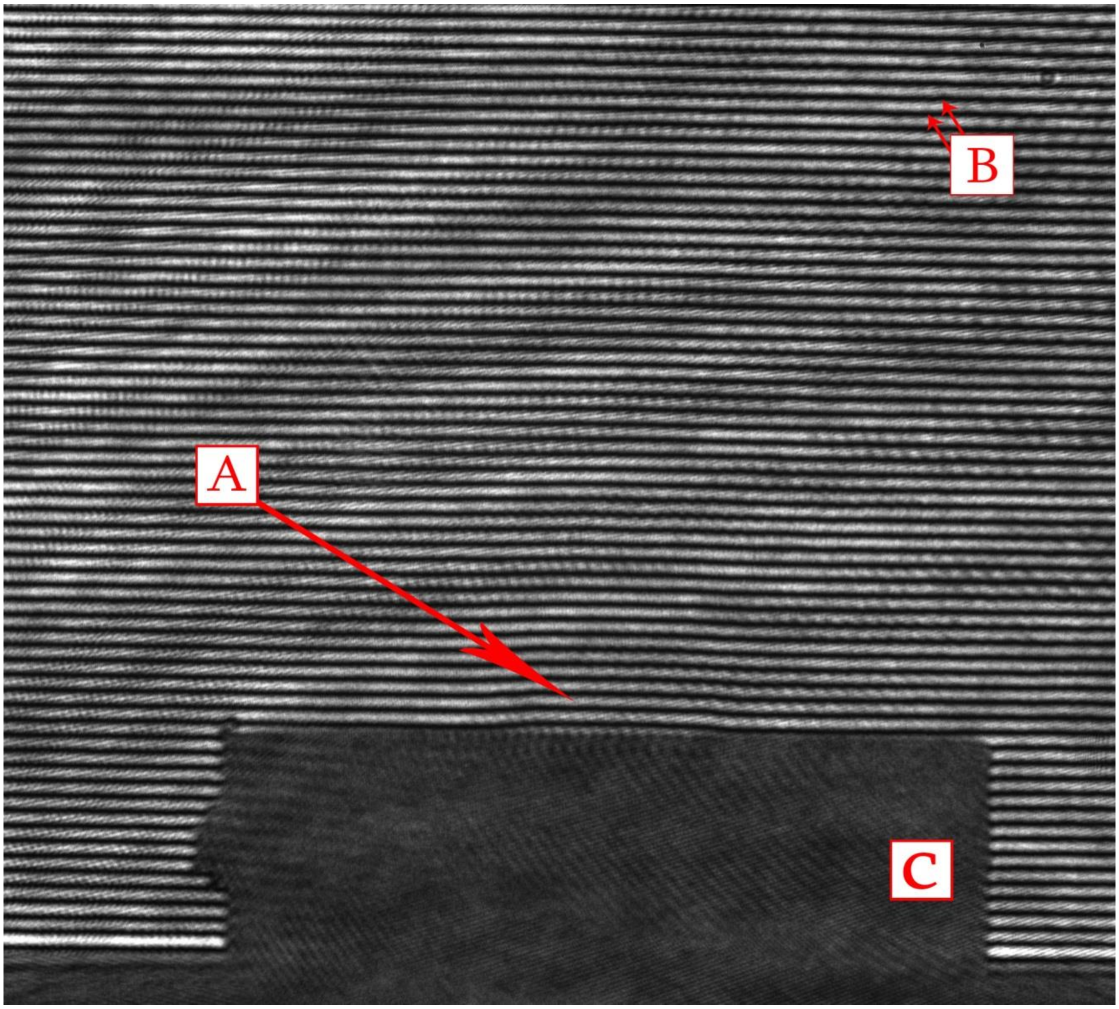

Figure 2.2: Interference pattern recorded by the camera: A) fringe shift. B) horizontal fringes, formed on the image, C) shadow of the attached µm nozzle.

If the gas jet is installed and expands into vacuum, a change of the local particle density, *i.e.* the refractive index, occurs. That is why, at the location of a varying particle density a fringe shift is formed, due to an angular phase shift. The refractive index depends on the gas density via the Clausius-Mosotti relation

$$\frac{\eta^2-1}{\eta^2+2}=\frac{n}{3}\gamma_{\mathrm{m}} \quad , [2]$$

where η symbolizes the refractive index, n is the particle density and γ_{m} is the molecular polarizability of the gas. If the approximation $(\eta^2-1)/(\eta^2+2)\approx 2/3(\eta-1)$ will be done the relation transfers to the Gladstone-Dale relationship, which can be given by:

$$\eta-1=\mathrm{K}n \ ,$$

The Gladstone-Dale relationship is very useful and easy to use for gases, because the constant K can be calculated for each gas if one of the values are known from η and n.

After description of the dependence between refractive index and the gas density, the gas density is calculated in the following section.

2.2. Abel Inversion

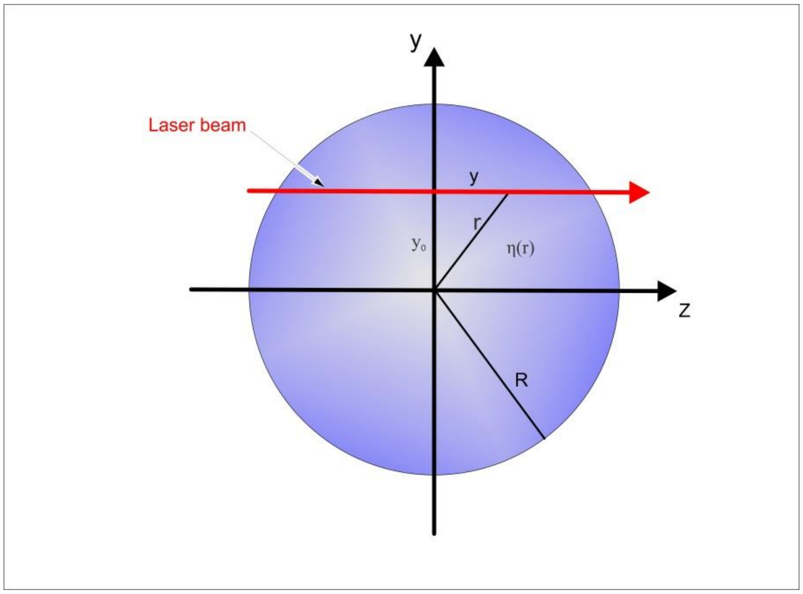

Figure 2.3: Schematic illustration of the phase shift along the *z* axis and the connection with the radial axis.

As it is known angular phase shift of fringes, $\vartriangle \Phi(x,y)$ depend on the electron density gradient if the laser beam propagates through the gas jet. It can be calculated by the integration along the HeNe Laser propagation phase:

$$\vartriangle \Phi(x,y) = \frac{2\pi}{\lambda_{\mathrm{L}}} \int_{\mathrm{z_0}}^{\mathrm{z_0}} \mathrm{d}z \left(1 - \eta(x,y,z)\right) \quad , [3]$$

with $\eta(x,y,z) \neq 1$ as the refraction index of the cylindrically symmetrical gas jet, and the borders of integration $\mathrm{z_{i,o}}$ as the entry and exit point of the Laser beam, respectively.

The changing of the Cartesian coordinates with cylindrical coordinates gives the following formula with the substitutions $r^2 = y^2 + z^2 \leftrightarrow z = \sqrt{r^2 - y^2}$ and $dz = r\,dr/\sqrt{r^2 - y^2}$

$$\vartriangle \Phi(x,y) = \frac{2\pi}{\lambda_{\mathrm{L}}} \int_{\mathrm{y_0}}^{\mathrm{R}} \mathrm{d}r \; \frac{r\,\overbrace{(1 - \eta(x,r))}^{\Delta\eta(x,r)}}{\sqrt{r^2 - y^2}} \quad ,$$

the distribution $\Delta\eta(x,r) = 1 - \eta(x,r)$ can be inverted if the electron density n_{e} is cylindrical. The Abel inversion can be written as:

$$\Delta\eta(x,r) = \frac{\lambda_{\mathrm{L}}}{2\pi^2} \int_{r}^{\mathrm{R}} \mathrm{d}y \frac{\partial \vartriangle \Phi(x,y)}{\partial y} \frac{1}{\sqrt{y^2 - r^2}} \quad ,$$

with the help of equation

$$\eta_{\mathrm{p}} = \sqrt{1 - \left(\frac{\omega_{\mathrm{p}}}{\omega_{\mathrm{L}}}\right)^2} = \sqrt{1 - \frac{n_{\mathrm{e}}}{n_{\mathrm{c}}}} \quad , [4]$$

$n_{\mathrm{e}}(x,r)$ can be defined as :

$$n_{\mathrm{e}}(x,r) = n_{\mathrm{e}} \cdot \left[1 - \left(\frac{\lambda_{\mathrm{L}}}{2\pi^2} \int_{\mathrm{r}}^{\mathrm{R}} \mathrm{d}y \frac{\partial \vartriangle \Phi(x,y)}{\partial y} \frac{1}{\sqrt{y^2 - r^2}}\right)^2\right] \quad .$$

Thus, $n_{\mathrm{e}}(x,r)$ depends on the location as well as on the variation of the phase shift $\vartriangle\Phi$ due to the electrons.

2.3. Data Analysis

The phase information is evaluated from the raw-data, *i.e.* the interferograms. The first step is a two-dimensional Forward Fast Fourier Transformation (2D-FFT), which requires an input field of a size $2^a x 2^b (a, b \in \mathbb{N})$. In the case of removing unoccupied pixels, the original 2D-data is set into the center of a field with next valid size and unoccupied pixels are filled with zeroes. Now, the 2D-FFT refers to the phase distribution of the interferograms. Using the primary intensity $I_0(r)$, the contrast of the interference fringes $m(r)$ and the phase distribution $\Phi\,(r)$, the spatial intensity distribution $I(r)$ can be written as:

$$I(r) = I_0(r) + m(r)\cos[2\pi v_0(r)r + \Phi\,(\mathrm{r})] \quad ,$$

The carrier frequency v_0 with parallel equidistant fringes superposes with the primary intensity and carries the interference pattern. The substitution $c(r) = {}^1\!/_2\, m(r)\mathrm{e}^{\mathrm{i}\Phi}$ refers to the complex notation

$$I(r) = I_0(r) + c(r)\mathrm{e}^{2\pi\mathrm{i}v_0 r} + \mathrm{c}^*(r)\mathrm{e}^{-2\pi\mathrm{i}\,v_0 r} \;,$$

After Fourier transformation this leads to:

$$\hat{I}(r) = \hat{I}(v) + \hat{c}(v - v_0) + \hat{c}^*(-v - v) \quad .$$

By cutting out the carrier frequency $\hat{c}^*$, the phase distribution $\Phi(\mathrm{r})$ can be filtered out of the interferogram, while the other values are set to zero. The phase distribution is defined by an Inverse Fourier Transformation:

$$\Phi\,(\mathrm{r}) = \arctan\frac{\mathrm{I_m}(c(r))}{\mathrm{R_e}(c(r))} \quad ,$$

where $\mathrm{I_m}(c(r))$ and $\mathrm{R_e}(c(r))$ are imaginary and real parts or complex numbers $c(r)$, respectively.

Because of the domain of definition [$-\pi, \pi$], phase shifts of $2\,\pi$ occur for $\Phi\,(\mathrm{r})$. Therefore, a saw tooth tread design of the stripe pattern results. With phase unwrapping it turns into a continuous profile. Here, neighboring pixels are being modulated until their phase gradient is minimized $< \pi$. The linearized phase must be substracted from the reference data avoiding the triggered gas jet.

At the end, the Abel inversion is related to electron density n_e in a specific distance above the nozzle. Thus, the data must be in symmetry of the center of the nozzle by averaging the data from the both side of the central axis. After taking the mean, the data are Abel inverted by an *f*-interpolation with a f-order polynomial function (particularly$= 2, 3$).

The refraction index is calculated in a following way:

$$\eta(r) = 1 - \frac{1\,\lambda_\mathrm{L}}{2\pi^2}\int_r^\mathrm{R} \mathrm{d}y \frac{\partial\Delta\Phi(\mathrm{y})}{\partial y}\frac{1}{\sqrt{y^2-r^2}} = 1 - \frac{\lambda_\mathrm{L}}{2\pi}\gamma\, a(r) \overset{!}{=} \sqrt{1-\frac{n_\mathrm{e}}{n_\mathrm{c}}}$$

$$\leftrightarrow n_\mathrm{e} = n_\mathrm{c}\cdot\left[1-(1-\tfrac{\lambda_\mathrm{L}}{2\pi}\gamma a(r))^2\right] \;\; ,$$

where $a(r)$ -is the factor of the local phase, and γ is a geometric imaging factor which can be determined by the known diameter d_n of the nozzle and number of pixels Z of the CCD camera.

for the interferometrical characterization of the nozzles, argon gas was used. The derivation for the gas density is similar to the one for plasmas, which can be defined by

$$\eta_\mathrm{gas} - 1 = \frac{1\,\lambda_\mathrm{L}}{2\pi^2}\int_r^\mathrm{R} \mathrm{d}y \frac{\delta\Delta\Phi(\mathrm{y})}{\delta y}\frac{1}{\sqrt{y^2-r^2}} = \frac{\lambda_\mathrm{L}}{2\pi}\gamma\, a(r) \overset{!}{=} (\eta_\mathrm{Ar}-1)\cdot\frac{n_\mathrm{gas}}{n_0}$$

$$\leftrightarrow n = n_\mathrm{gas} = \tfrac{\lambda_\mathrm{L}}{\pi}\,\tfrac{n_0}{\eta_\mathrm{Ar}-1}\gamma\, a(r) \;\; , [6]$$

where $n = n_\mathrm{gas}$ is neutral gas density , n_0 is the density of atoms at the standard temperature and pressure and it is equal to $2.68 \cdot 10^{19}\ \mathrm{atoms}/cm^3$, and $\eta_\mathrm{Ar} = 1.000284$ is the index of refraction of argon for a wavelength of λ_L=632.8 nm.

For a nozzle of the *Parker Hannifin series 9* valve with an outer diameter of $d_{\mu\text{m-nozzle}} = 1490$ µm and $Z_{\mu\text{m-nozzle}} = 1395$ pixel, γ can be calculated to $\gamma_{\mu\text{m-nozzle}} = 11 \cdot 10^{-7}$ 1/m, *i.e.* 1 pixel corresponds to 1.1 µm.

3. Interferometrical Characterization of the Density Profile

In order to get detailed information of the density profiles of a gas jet, the attached µm-nozzle has to be characterized interferometrically. In the framework of this thesis, a Mach-Zehnder interferometer was used for this purpose. In the first subsection the experimental setup is described in detail, while the second one deals with the implementation of the measurements. Finally, in the last subsection the analysis of the received data is illustrated.

3.1. Experimental Setup

The experimental setup, which was built up at the Central Institute of Engineering, Electronics and Instrumentation (ZEA-1) of the Forschungszentrum Jülich, is situated on an optical table, which is high stable and thus it is guaranteed that external factors will not affect the experiment.

On the optical table a cylindrical linearly polarized 15 mW HeNe laser (safety class 3B / lllb) with a wavelength of $\lambda = 632.8$ nm, an $1/e^2$ beam diameter of 1 mm and a polarization ratio of > 500:1 is mounted. The HeNe laser is manufactured by *Linos GmbH,* a global German manufacturer of sophisticated optical components and a member of the *Qioptiq Group* since 2006. [7] The outcoming laser beam has a divergence of 1 mrad and when used in warm condition the pointing stability is < 0.005 mrad.

In order to generate a clean, spatially uniform and Gaussian beam, directly on the orifice outlet at the laser's front side a beam expander system (25 x) with an additional spatial filter are attached. The input of the system consists of a diffraction-limited aspheric lens (translation along the *z*-axis, *i.e. the optical axis,* possible). The original Gaussian laser beam has spatially varying intensity noise. When this beam is focused by an aspheric lens, the incoming beam is transformed into both a central Gaussian spot (the *z*-axis) and side fringes, *i.e.* the unwanted noise. The radial position of the side fringes is proportional to the spatial frequency of the noise. Afterwards, the beam is focused through a pinhole with a diameter of 20 µm, which is mounted in an *x*-*y*-translator. Thus, the clean central Gaussian spot can pass while the fringes are blocked. Behind the spatial filter, the laser beam is expanded by a factor of 25 times.

In the following subection, the fine adjustment of the spatial filter is described in detail.

3.1.1. Fine adjustment of the spatial filter

First of all, the beam expander system has to be unmounted into three basic components A, B, and C (*cf.* Fig. 3.1). A and B contain the aspherical lens and the pinhole of the spatial filter unit, while C is the telescope of the beam expander unit. In a first step, A and C are connected and the beam entrance component is centered to the laser beam with the help of two 2 mm hexagon socket screws (A1, A2). After a homogeneous distribution can be observed at the beam exit side, component C is exchanged with component B. With the tubular key (a special key provided with the system), the inner mount of the spatial filter is rotated by one turn. This rotation leads to a translation of the pinhole in *z*-direction, *i.e.* the distance between the focal spot and the pinhole is changed. By turning the screws B1 and B2, the position of the pinhole is changed along the *x*- and *y*-axis until the laser beam can propagate through the orifice with a maximum of brightness. Afterwards, the optimal focus has to be adjusted by turning the inner mount back in *z*-direction till no diffraction rings can be observed on a screen behind the spatial filter. A stepwise readjustment of the screws B1 and B2 is necessary to keep the pinhole centered.

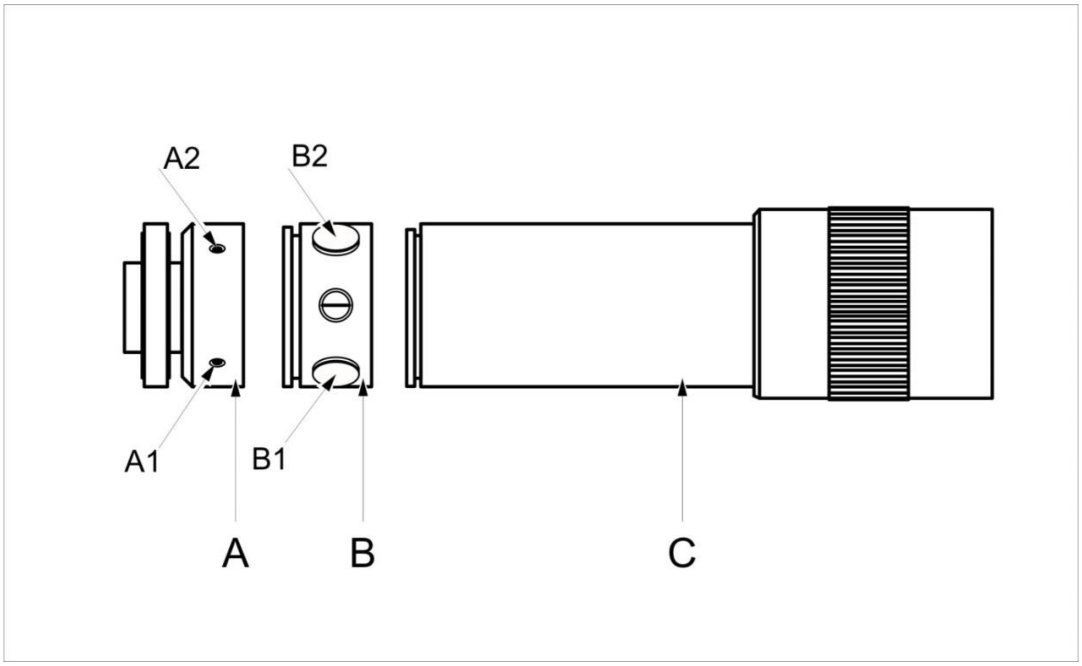

Figure 3.1: Beam expander scheme. A and B contain the aspherical lens and the pinhole, C is the telescope.

Finally, component C is mounted back on component B and the fine adjustment of the beam expander is completed. Now, a clean, spatially uniform and Gaussian beam with a beam diameter of 25 mm is given.

Due to the fact that it is not clear in which direction and in which angle the expanded laser beam exits the HeNe laser, a fix optical axis has to be defined. In the following subsection, this adjustment is described in detail.

3.1.2. Definition of the optical axis

After the laser beam has been expanded, the next step is to define the optical axis. For that purpose, two completely closing iris diaphragms (max. aperture diameter of 30 mm) are installed behind two silver circular plane mirrors (size of 2"). The optical axis is defined by the apertures. With the first mirror (Mirror 1, *cf*. Fig. 3.2) the laser beam is centered on the first iris diaphragm and an adjustment of the second mirror (M2) reflects the beam on the second one, respectively. By iteration of height and side adjustments at each mirror, the laser beam can propagate along the optical axis and enters the Mach-Zehnder interferometer which is described in the following paragraph.

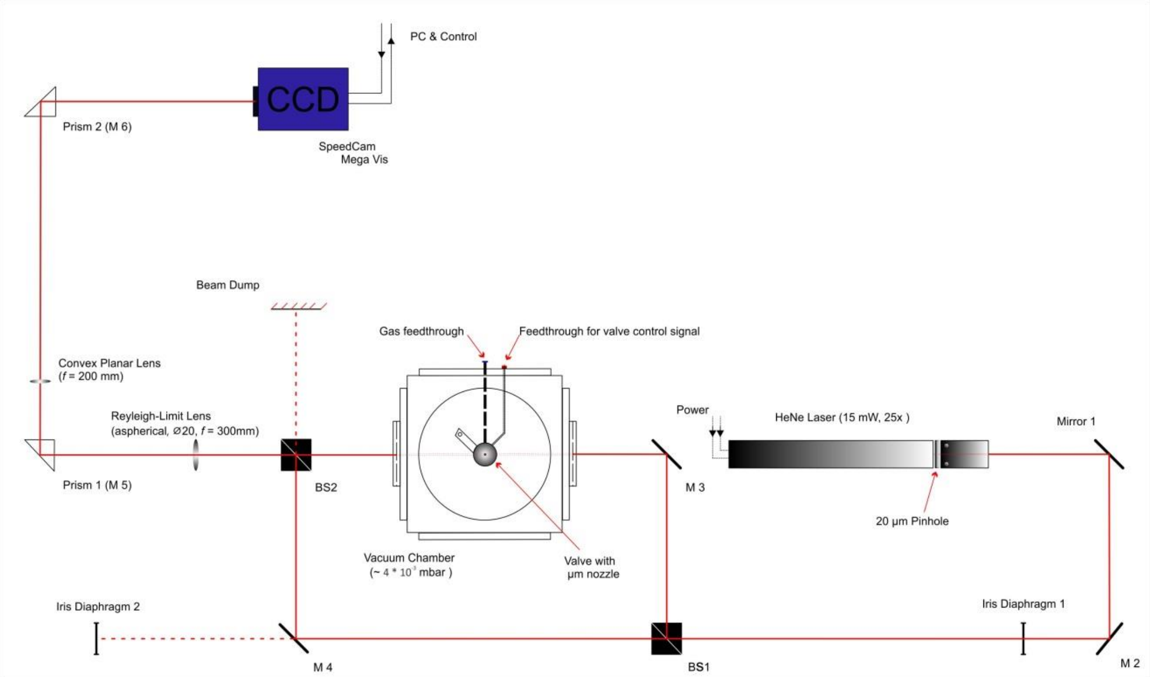

Figure 3.2: Scheme of the full experimental setup.

3.1.3. The Mach-Zehnder interferometer

As it is said in Sec. 2.1, the functional principle of a Mach-Zehnder interferometer is based on superposition of two beamlets. If both beamlets with the same phase propagate through media with different reflection indices η and are brought together, they interfere and an interference pattern is formed. The refraction index and also changes of the refraction index can be detected and calculated.

With the help of a non-polarizing 50:50 1" beam splitter cube the widened laser beam is split into two equal beamlets. One beamlet is propagating through air and serves as a reference beam. The other one enters the vacuum chamber and illuminates the tip of the µm-nozzle.

The minimal diameter of the Laval shaped nozzle is 167 µm (*cf.* Fig. 3.3). The nozzle is used to build up a hot pressurized gas jet expanding with supersonic speed and an adequate density profile.

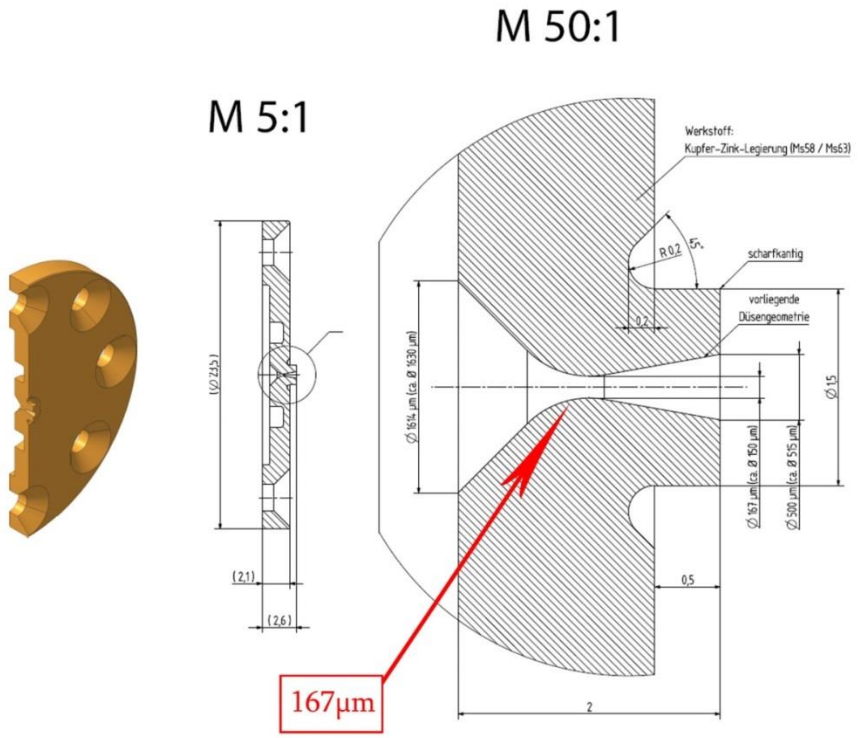

Figure 3.3: Laval shaped µm-nozzle. [8]

The µm-nozzle is attached on the *Parker Hannifin series 9* valve, a fast-opening solenoid pulse valve which is constructed of non-corroding, passivated stainless steel (*cf.* Fig. 3.4.). The valve operates at repetition rates of up to 12 Hz and backing pressures of up to 86 bar, while response times of a few µm can be adjusted. This type of solenoid valves is able to combine high speed, ultra-low leak rates, high flow and high temperature capability in a small size. Inside the valve body, an armature is pulled downwards. At the end of it, a Teflon poppet is attached which seals the valve orifice in the case of a closed valve. [9]

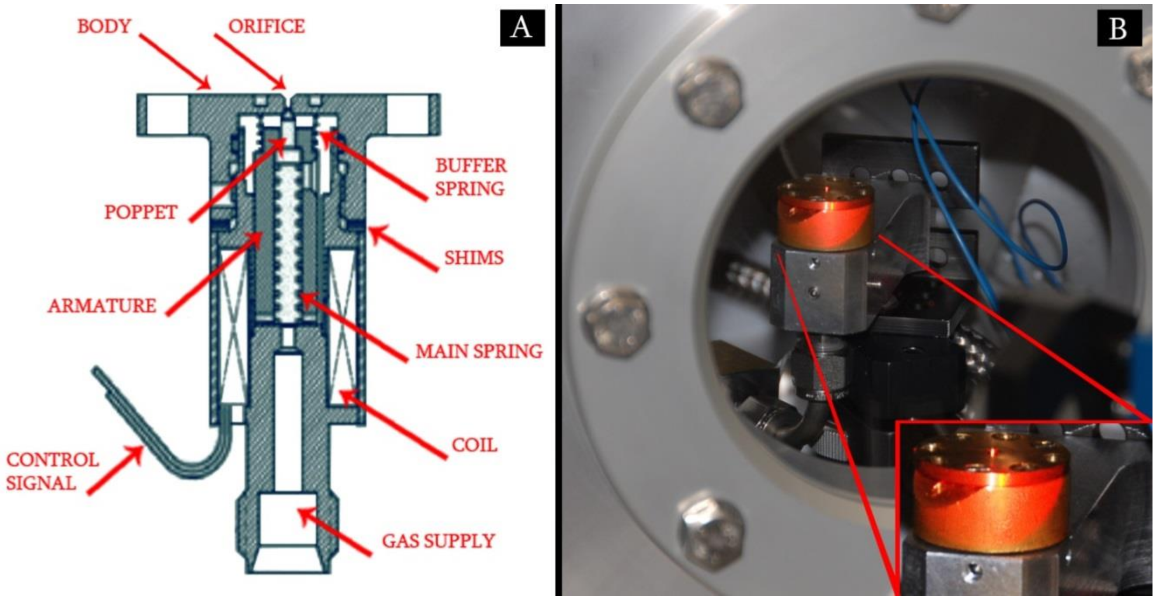

Figure 3.4: The *Parker Hannifin series 9* valve: A) cross section of the *Parker Hannifin series 9* valve, B) *Parker Hannifin series 9* valve with Laval shaped µm-nozzle. [9]

In order to protect the µm-orifice of the attached nozzle from blinding due to impurities out of the tube system of the gas supply, a sintered filter is installed directly in front of the valve’s gas inlet. Figure 3.5 illustrates the orifice of the µm-nozzle after using it with and without such a sintered filter. As it can be regarded, burrs and splinters from the vacuum tubes totally clog the nozzle.

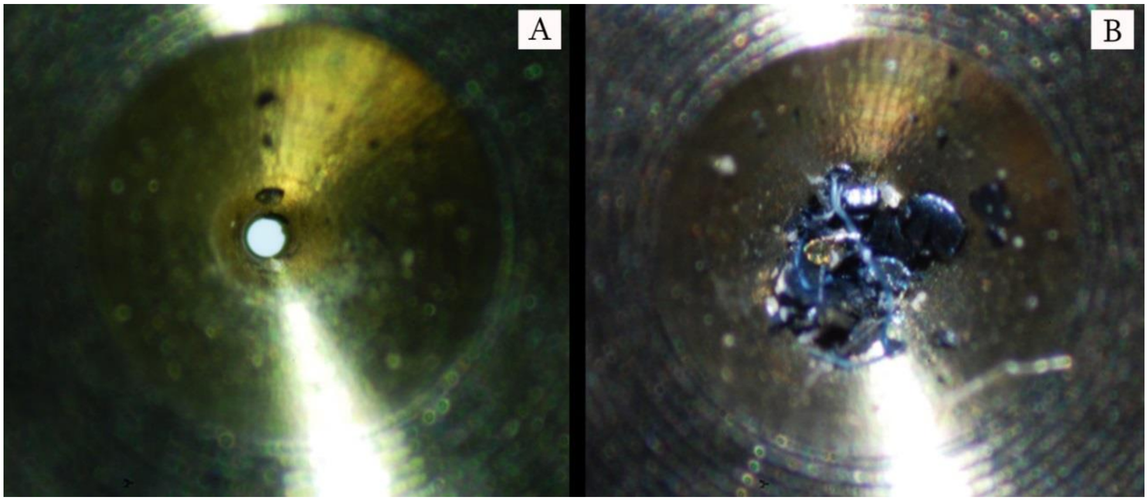

Figure 3.5: µm-nozzle orifice: A) with sintered filter, B) without sintered filter. [10]

The vacuum chamber is an aluminum cube with a feed size of 250 mm. At each lateral face an O-ring sealed flange with circular cross section can be mounted with 8 mm hexagon socket screws. In laser-propagation direction two windows with a diameter of 160 mm are mounted in order to let the second beamlet pass the vacuum chamber. On the top of the vacuum chamber, there is a feedthrough for the pumping system, while on the right side an electrical feedthrough for the valve and a feedthrough for the argon gas supply are given. The attached vacuum pump creates a vacuum of approximately $4x10^{-3}$ mbar.

After the second laser beamlet passes the vacuum chamber, the two beamlets superpose in the second beamsplitter (non-polarizing, 50:50, 1"). The combined beam propagates through an aspherical Reyleigh-limit lens with a focal length of f = 300 mm and a diameter of 20 mm. Afterwards, the beam goes through a convex plan lens (with a focal length of f = 200 mm) and finakky it falls on the CCD camera sensor.

The CCD camera is a *SpeedCam Mega Vis* manufactured by the *High Speed Vision GmbH*. With its high speed CMO sensor (11 x 11 µm, 22.18 x 22.18 mm, a diagonal of 31.36 mm) the camera is a powerful device for recognizing and recording data in a high resolution. It is able to record movies (color depth: 12-bit monochrome) during 3.1 s and a fast Gigabit Ethernet port provides to transfer information to the computer quickly [11] . For a better understanding of how the above described interferometer and whole experimental setup works, in the following subsection, the measurement process is described in detail.

3.1.4. Measurements

The measurement starts with a set of parameters. It is necessary to make notes before and after the measurement. Furthermore, it is very important to take in mind which devices are used during the process and also which materials of devices if it impacts on the measurement result.

The measurement performed with argon gas, supplied from cylindrical gas bottle. The container can hold a pressure of up to 200 bar. The measurements are done at various system pressures and hence, it is necessary to control them precisely. A specially made big manometer (*cf.* Fig. 3.6.) is served as a high pressure control (*e.g.* 250 bar). It has several gauges for more precision and ease of use.

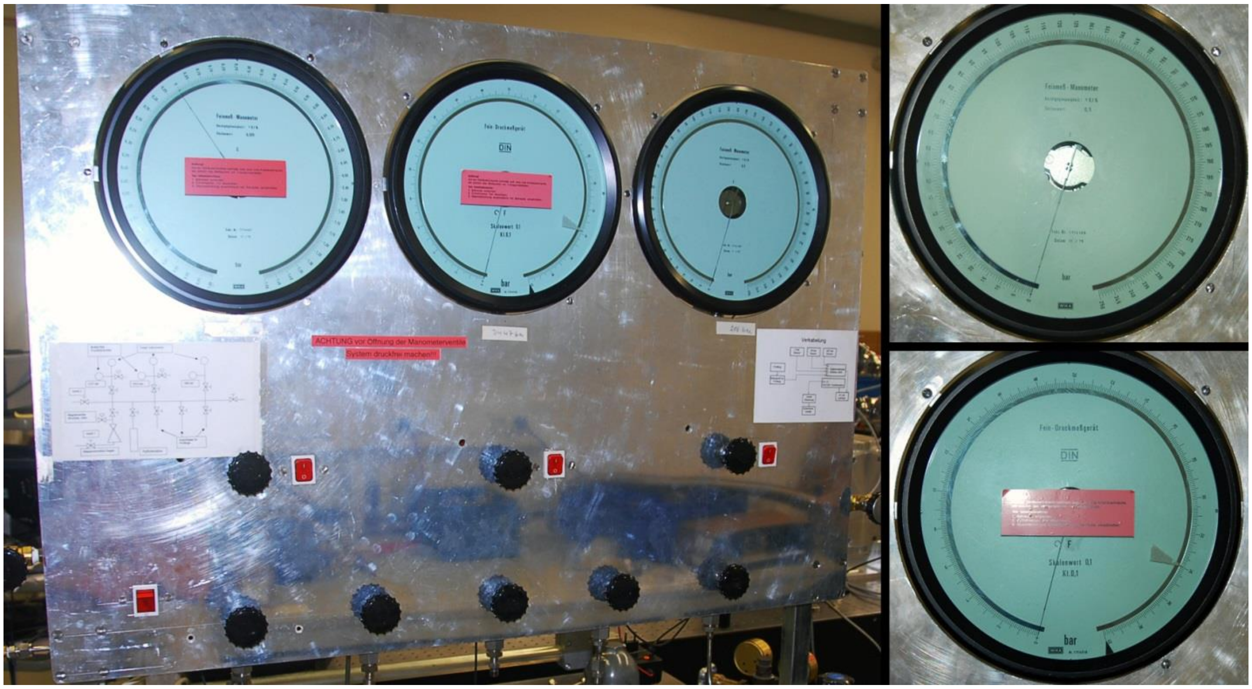

Figure 3.6: Special made big manometer.

Finally the gas guided to the valve through a semi-flexible tube with an included gas filter in the middle of it. The gas connection tube is made of stainless steel and has a diameter of 0.4 cm. The volume of the connection tube (including different sized volumes of the filter and manual valves) is 80 cm^3 and it is permanently controlled with a pressure transducer.

On the other hand, any valve operation happens inside the vacuum chamber, which is made of aluminum (chamber with a volume of ~14038 cm^3). The vacuum is provided and stabilized with a turbo pump and a compact full range gauge, with a pressure range from 5 x 10^{-9} to 1000 mbar. This “couple” holds the vacuum up and is able to renew the pressure after each valve operation.

Results of the experiment are recorded by a CCD camera, which for the current experiment is the SpeedCam Mega Vis (*cf.* Fig. 3.7.). This powerful device with a fast 22.18 x 22.18 mm sensor and a Gigabit Ethernet connection to the operation computer records a movie, instead of single pictures.

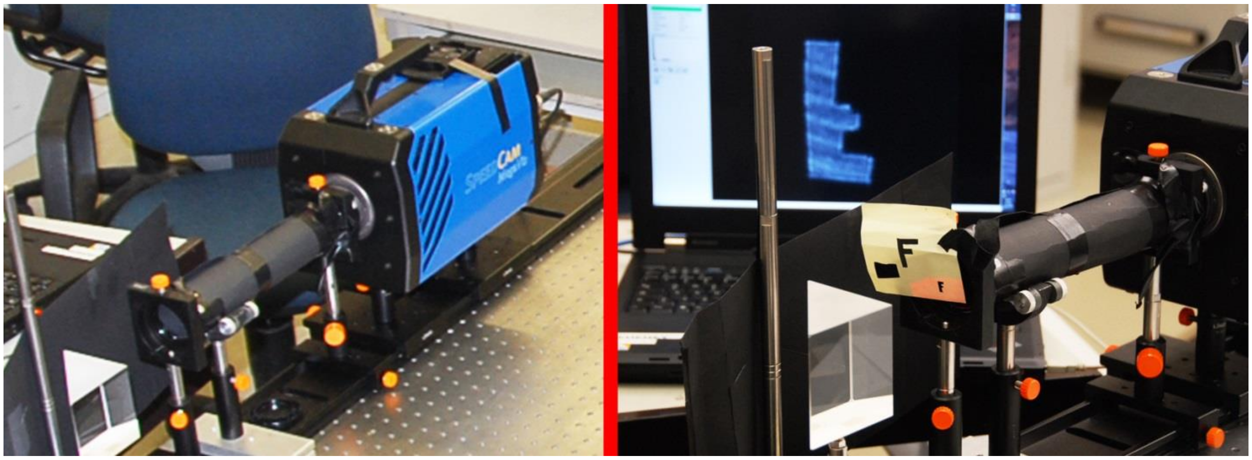

Figure 3.7: SpeedCam Mega Vis.

Taking pictures continuously in a movie is a very important function for the being experiment choosing the most useful picture for further analyses is possible. The recorded movies can be exported in single pictures in a *.TIF (Tagged Image File Format) format by using the CamControl basic software. Both the camera and the valve are triggered. The triggering process is managed by a stanford box and can be monitored with the transient recorder. The stanford box simultaneously generates trigger signal for each CCD and IOTA ONE pulse driver.

The IOTA ONE pulse driver is used to control the valve’s opening and closing time. It makes microsecond or millisecond pulses and also pulses with the length of minutes. The transient recorder is a powerful Windows XP based machine with 8 channels for get-transfer information and software (*e.g. Trans AS 3.0* from *Elsys AG*) for quickly processing data. It is important to mention, that the camera starts recording before the valve is opened and stopped. This ability makes it easy to observe the full range of the gas motion, from the start to the end.

After this brief description of the measurement process, a concrete example, which was done with a system pressure of 40 bar, is presented.

A regular argon system pressure of 40 bar is set with the manometer, which is supplied to the valve. The valve is fully closed and waiting for the action signal, while the turbo pump creates a vacuum inside the vacuum chamber. The created vacuum inside the chamber is $6.8 \cdot 10^{-3}$ mbar. After regulation of gas pressure and vacuum, it is time to trigger the CCD camera and set valve opening time on the IOTA ONE. This process was done under the control of the transient recorder. In Figure 3.8 it is possible to see a screenshot which was taken during the triggering process. The valve operation time was set to 1 millisecond. After adjusting the parameters on the CCD camera (*e.g.* a frame rate of 5800 fps), and everything is ready for starting the measurement.

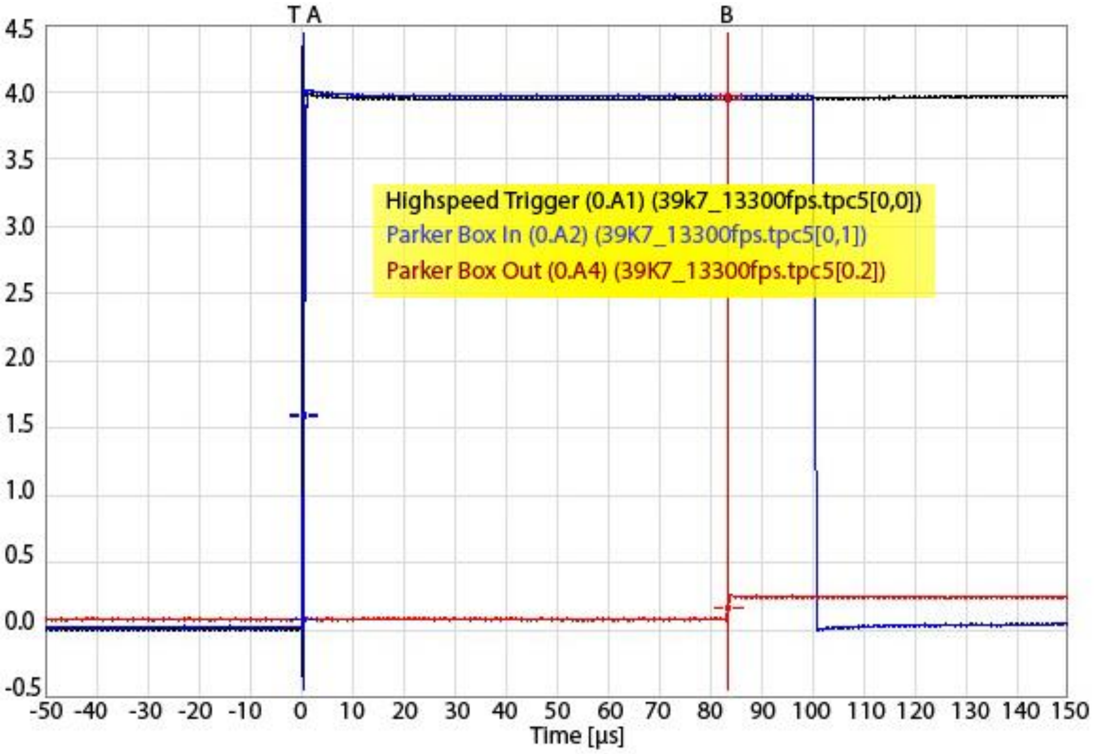

Figure 3.8: Screenshot of the “transient recorder”. [10]

After pushing the “execute” button at the Stanford box, a signal is created both for the pulse driver and for the CCD. Now, the pulse driver is generating an open and close pulse for the valve and a gas jet is built up, while the camera is making a movie. The movie is divided into the single pictures which are saved as *.TIF files. After the valve operation, a vacuum level change occurs and at this moment it is $5.2 \cdot 10^{-2}$ mbar. Finally, the turbo pump rebuilds the vacuum and the whole system is ready for new shots again.

Figure 3.9 illustrates the gas jet (B) which can be seen without any deep analysis. The gas jet was created with an attached argon pressure of 39. 9 bar and with a camera exposure time of 154 µs (camera pre-trigger of 2 %).

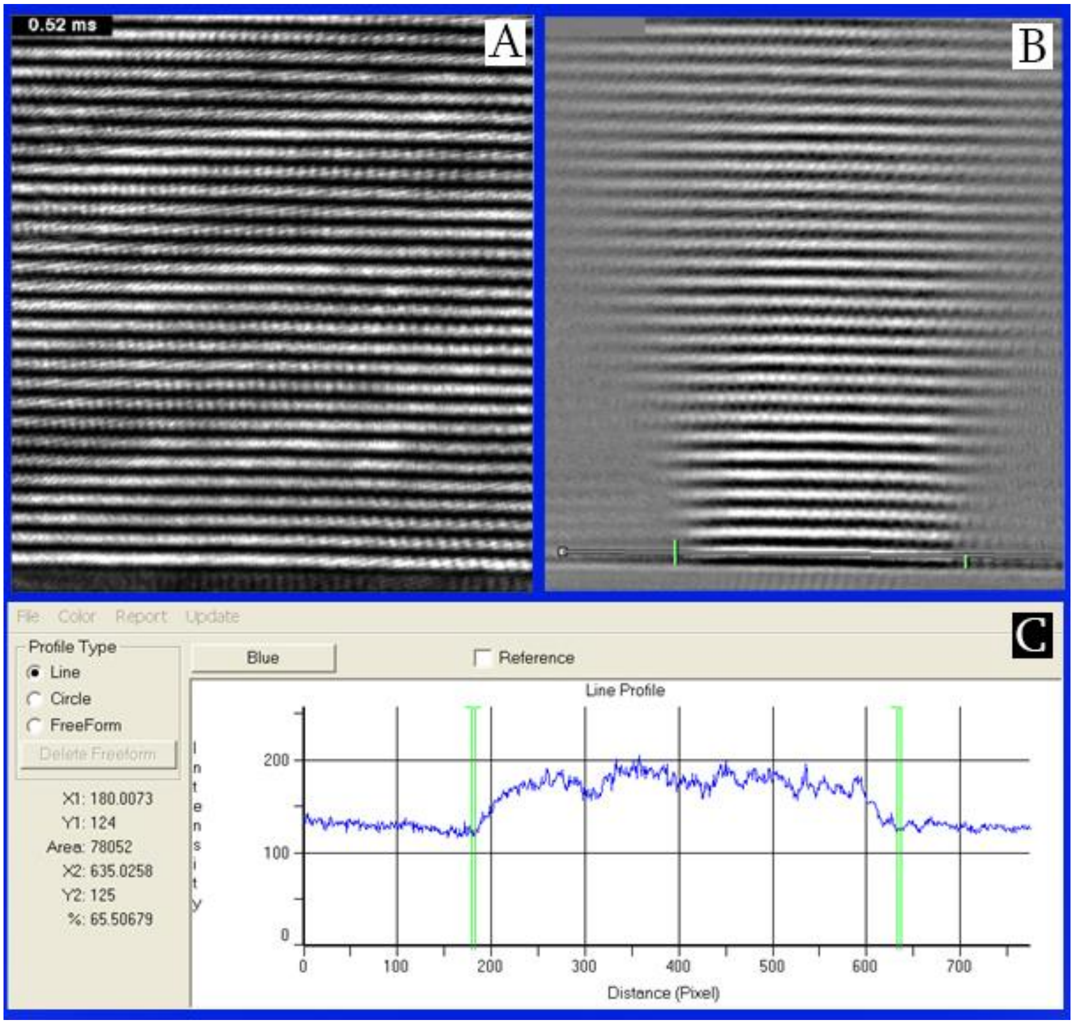

X1: 180.0073
Y1: 124
Area: 78052
X2: 635.0258
Y2: 125
%: 65.50679

Figure 3.9: Gas jet. A) Reference frame. B) Gas jet shape after the overlap and the difference between two frames with and without gas. [10]

3.2. Results of Analysis

It is very interesting to observe how the valve behaves for different pressures at a certain opening time. Therefore, the valve was characterized for several backing pressures from 3 bar up to 40 bar. The CCD camera starts with the movie record before the valve opens and stops the record after valve is fully closed. Afterwards, the movie is split into single pictures, with 0.83 ms timesteps by using the basic camera software. For all pressures, 5 ms was chosen for the camera buffer time and the total record continues for 25 ms, *i.e.* the time interval was set from - 5 ms to + 25 ms.

The recorded data was analyzed by using a *Matlab* code. For each pressure a height scan was done along the vertical central axis and two height scans were performed for horizontal axis (0 and 500 µm above the nozzle). Also the 2d particle density distribution was illustrated. It is very important to know the particle density for 500 µm above the nozzle tip, because it is the minimal height available for laser acceleration experiments.

First of all it is important to know what happens in a period when the valve starts to open until it is fully closed. This process is shown in Fig. 3.10, with 0.83 ms timesteps. Based on this Fig. it becomes clear that after 0.83 ms the valve is open and a first gas flow comes out. Next to it is possible to observe its behaviour till approximately 14.17 ms, when the gas flow is attenuated.

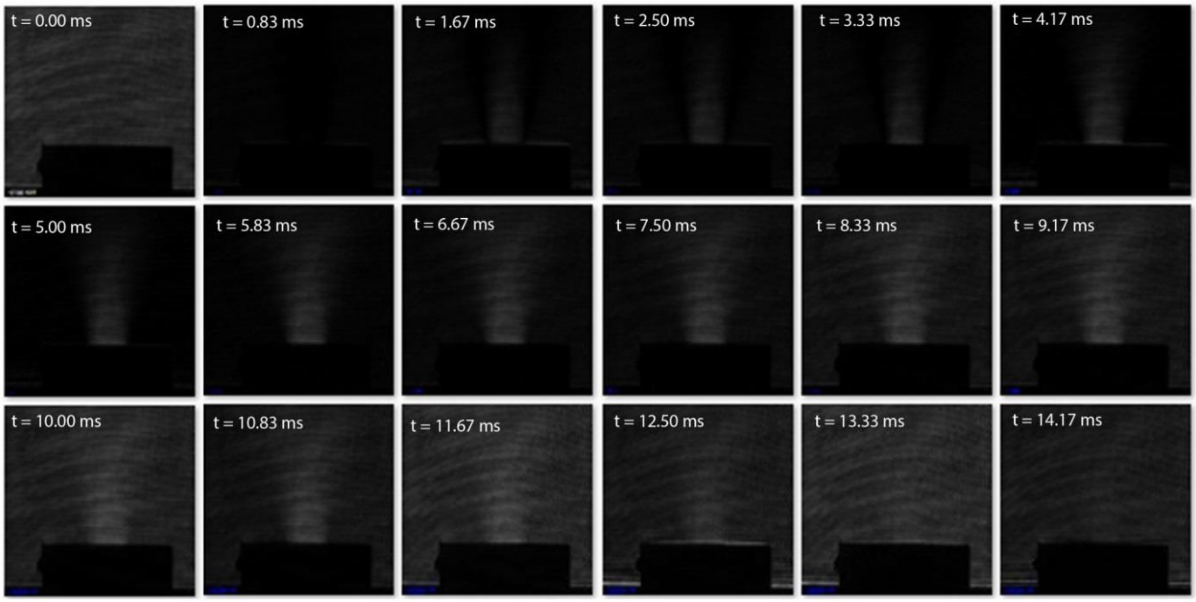

Figure 3.10: Qualitative analysis of the time-dependence of the density profile with Photoshop.

The results of the analyses for several argon pressures are described below. After this, it is possible to make a comparison between them.

40 bar, 3.33 ms after the trigger:

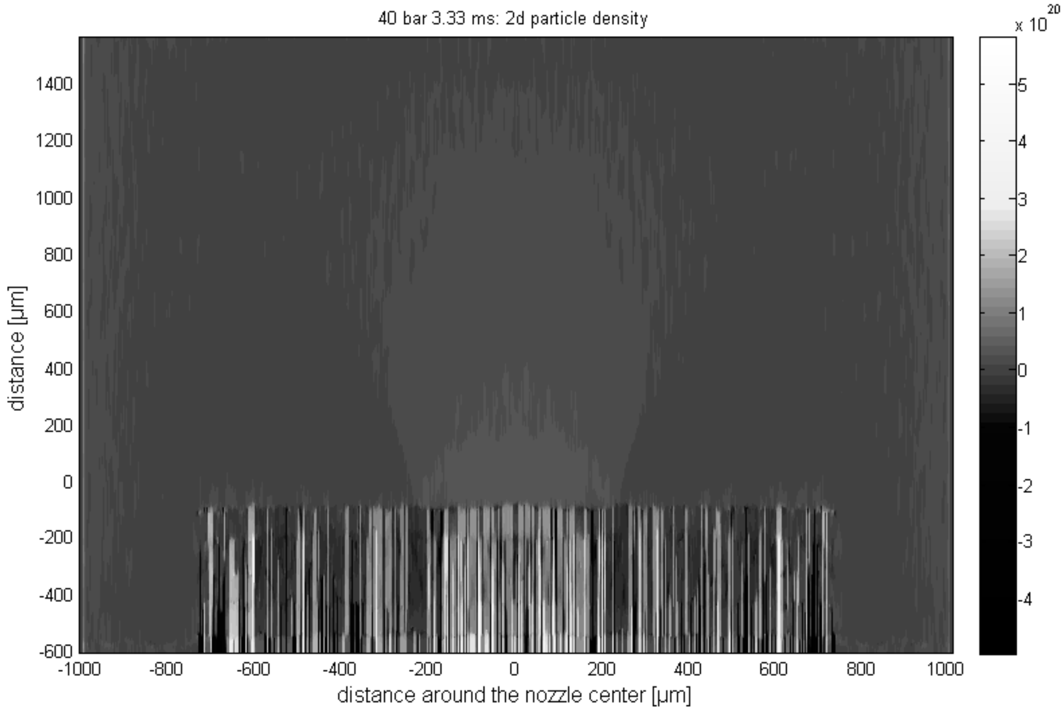

Figure 3.11: 2D particle density distribution.

Figure 3.11 represents particle density distribution in two dimensions. In this picture it is possible to make an imagination of gas jet shape, *e.g.* for 40 bar pressure the gas jet has a good and nice shape according to its height and width.

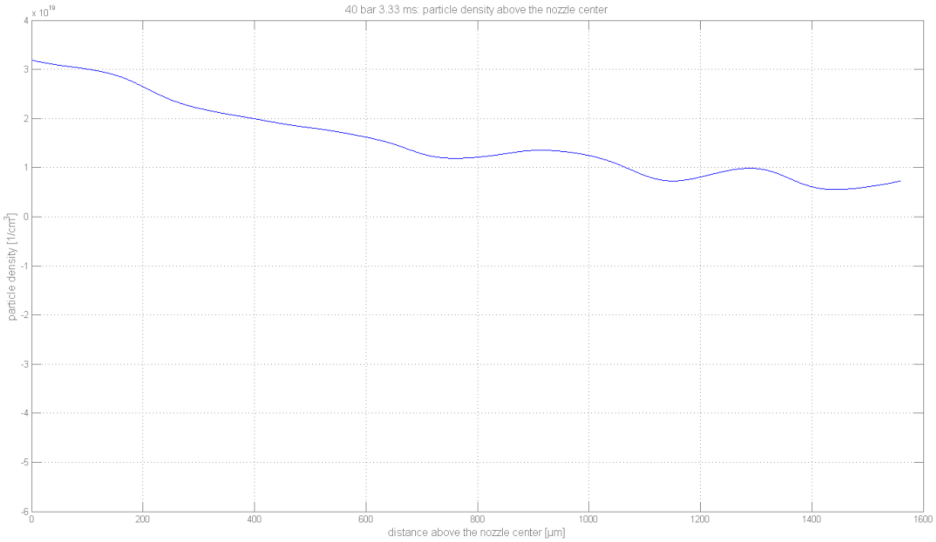

Figure 3.12: Height scan along the vertical central axis. The particle density changes not linearly from 0 µm to 1550 µm above the nozzle: 3.51 x 10^{19} – 0.2 x 10^{19} particles/cm^3).

Figure 3.12 is the result of a height scan along the central vertical axis. It becomes obvious that when the height is incremented from the nozzle, the particle density decreases not linearly. For 40 bar , the particle density for 0 µm above the nozzle is $3 \cdot 10^{19}$ particles /cm^3, and even for 1550 µm height above the nozzle the particle density is $0.2 \cdot 10^{19}$ particles/cm^3.

Figures 3.13 and 3.14 are the height scans along a horizontal axis, for 0 µm and for 500 µm above the nozzle, correspondingly.

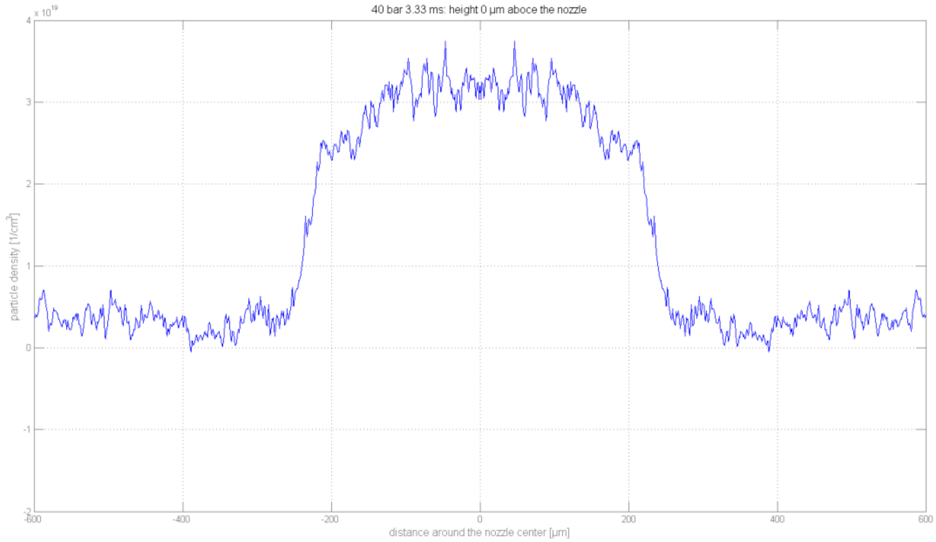

Figure 3.13: Height scan along the horizontal axis, 0 µm above the nozzle. The particle density has a maximal value of $3 \cdot 10^{19}$ particles/cm^3.

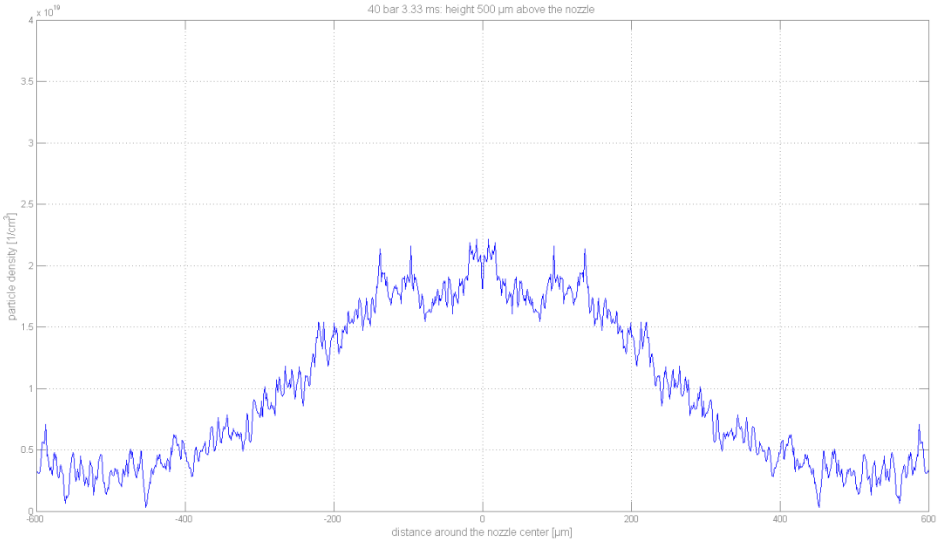

Figure 3.14: Height scan along the horizontal axis, 500 µm above the nozzle. The particle density has a maximal value of $2 \cdot 10^{19}$ particles/cm^3.

Their comparison makes clear that for the interesting height (500 µm above the nozzle edge) the particle density distribution has a broadened shape, while at 0 µm its edges are sharp and the central part is approximately plateau-like. Values for the particle density shown in Fig. 3.14 are approximately 34% smaller than in Fig. 3.13.

40 bar, 8. 33 ms after the trigger:

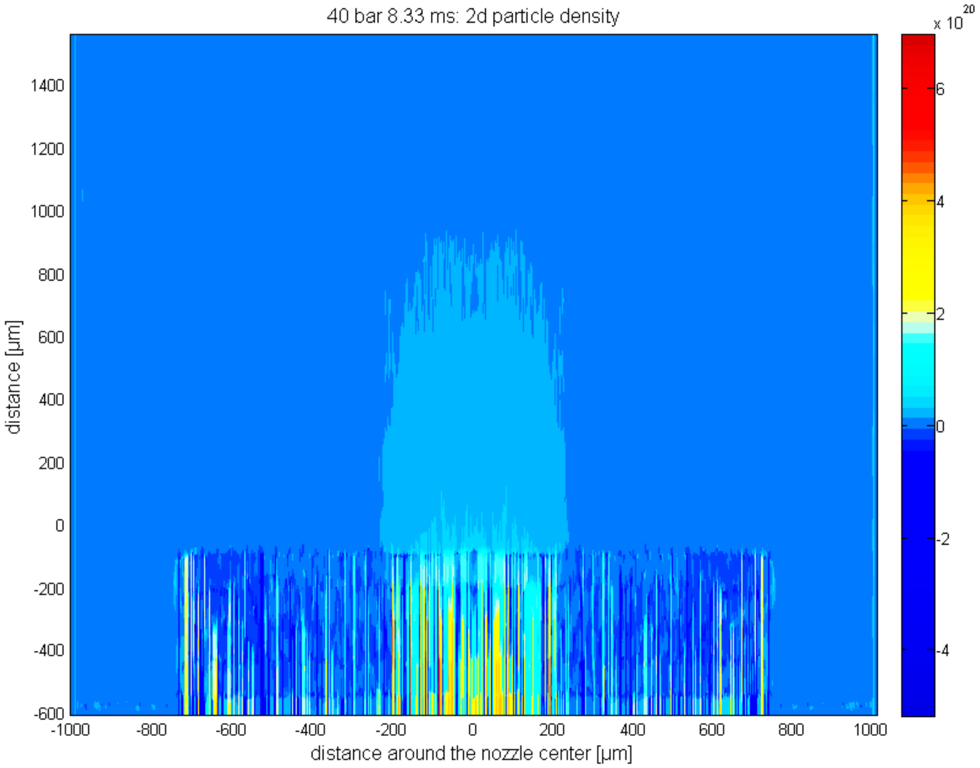

Figure 3.15: 2D particle density distribution.

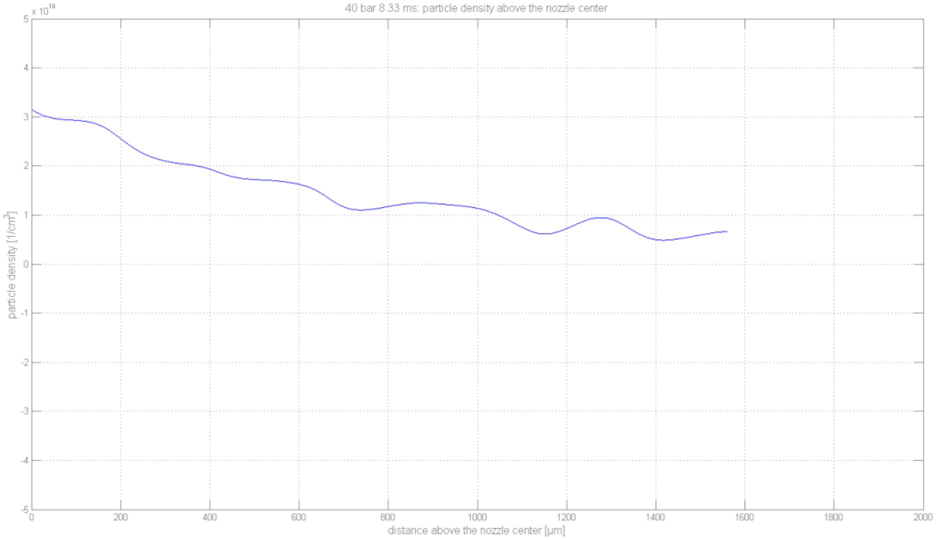

Figure 3.16: Height scan along the vertical central axis. The particle density changes not linearly from 0 µm to 1500 µm above the nozzle: 3.1 x 10^{19} – 0.5 x 10^{19} particles/cm^3).

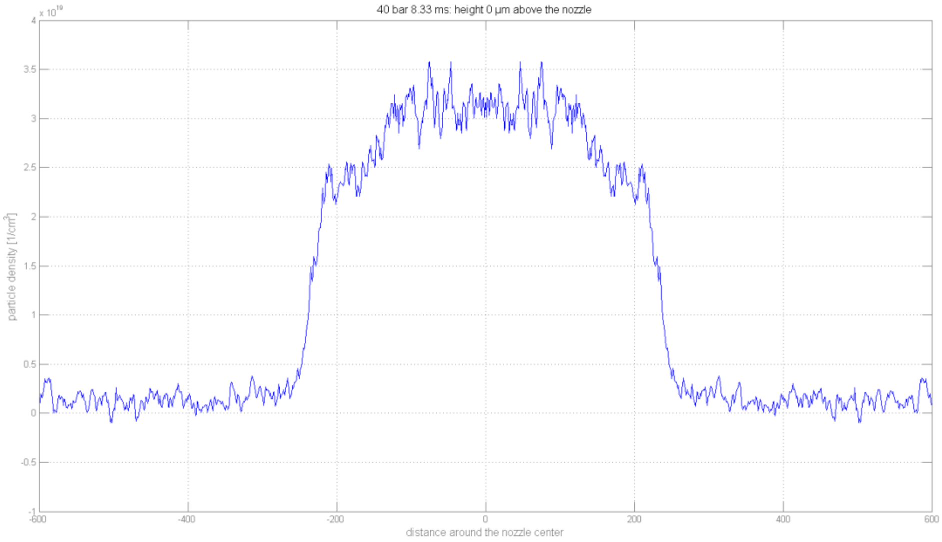

Figure 3.17: Height scan along the horizontal axis, 0 µm above the nozzle. The particle density has a maximal value of 3 · 10^{19} particles/cm^3.

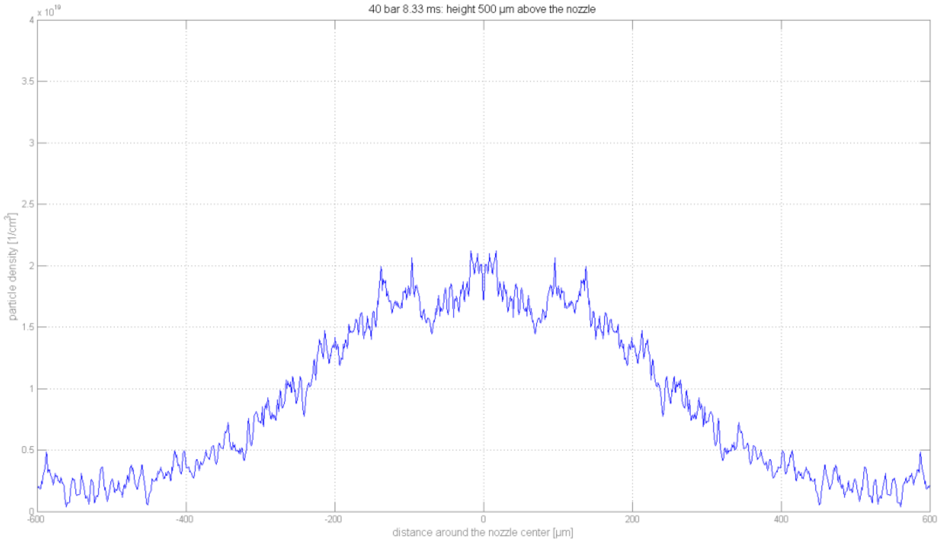

Figure 3.18: Height scan along the horizontal axis, 500 µm above the nozzle. The particle density has a maximal value of 2 · 10^{19} particles/cm^3.

The same data (only for 3.33 ms) are given on the next pages for the other argon pressures. These are only the basic data without further explanations.

30 bar, 3.33 ms after the trigger:

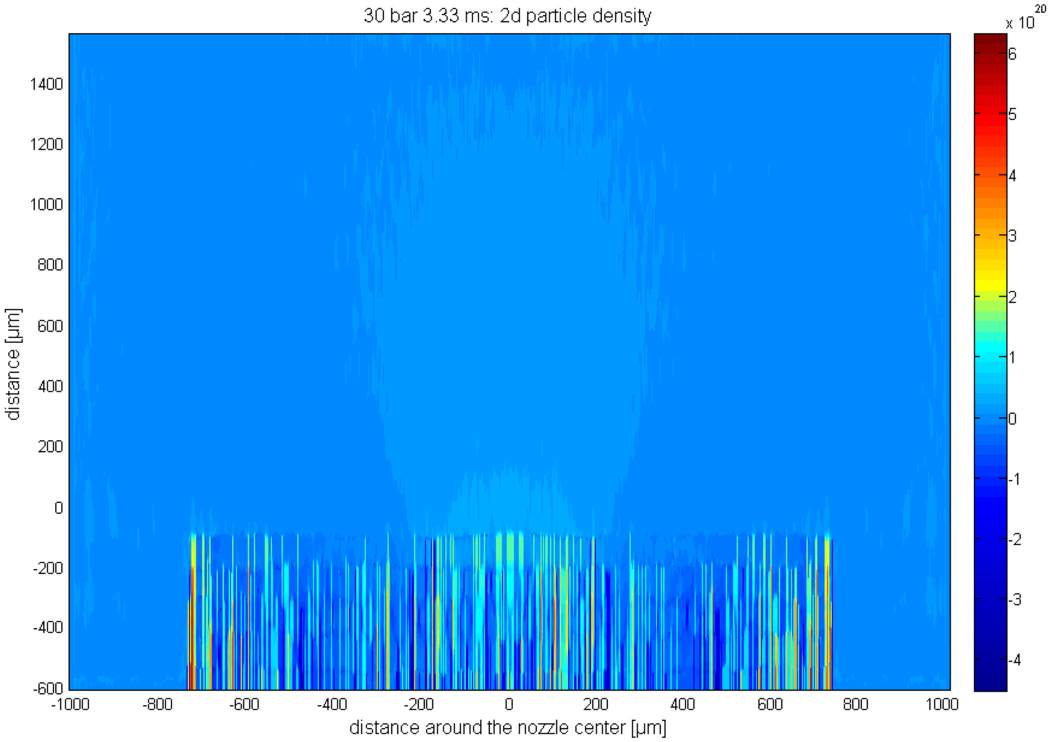

Figure 3.19: 2D particle density distribution.

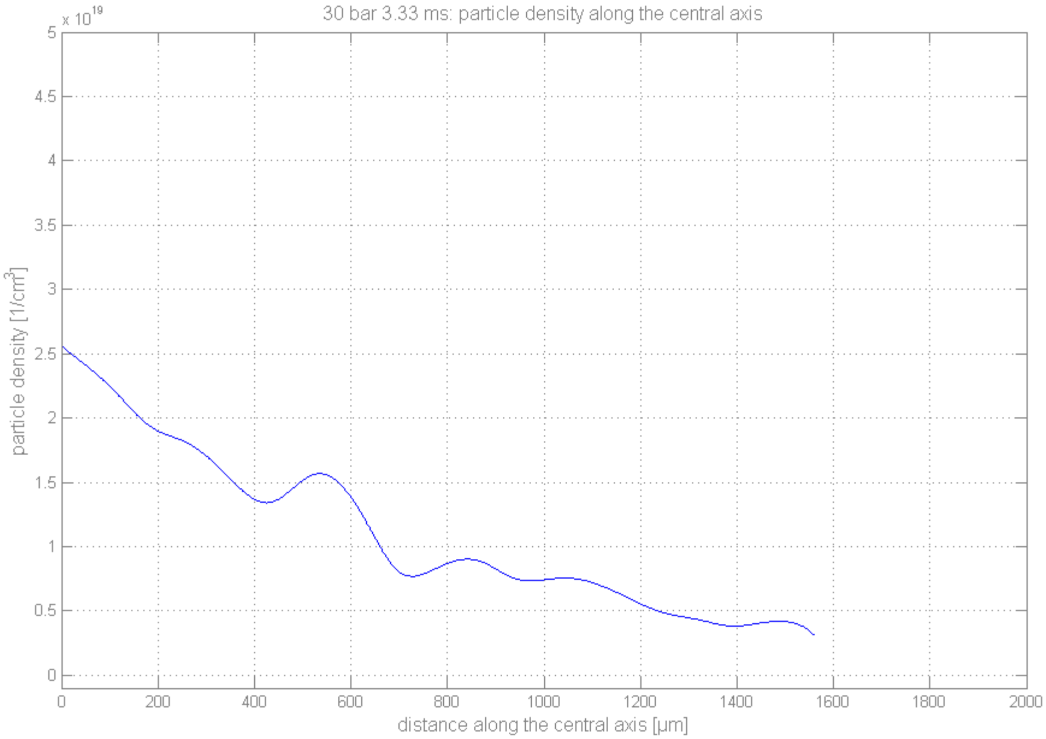

Figure 3.20: Height scan along the vertical central axis. The particle density changes not linearly from 0 µm to 1550 µm above the nozzle: 2.51 x 10^{19} – 0.31 x 10^{19} particles/cm^3.

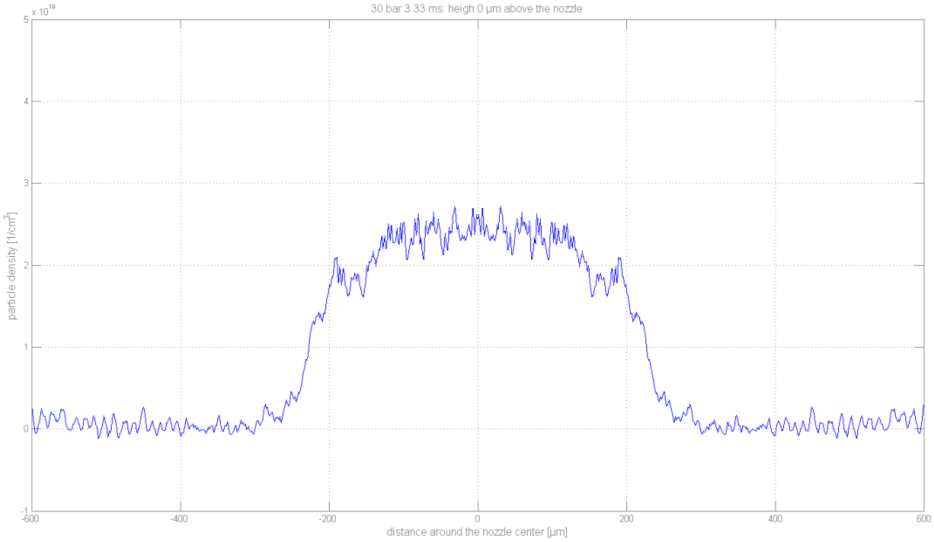

Figure 3.21: Height scan along a horizontal axis, 0 µm above the nozzle. The particle density has a maximal value of 2.51 x 10^{19} particles/cm^3.

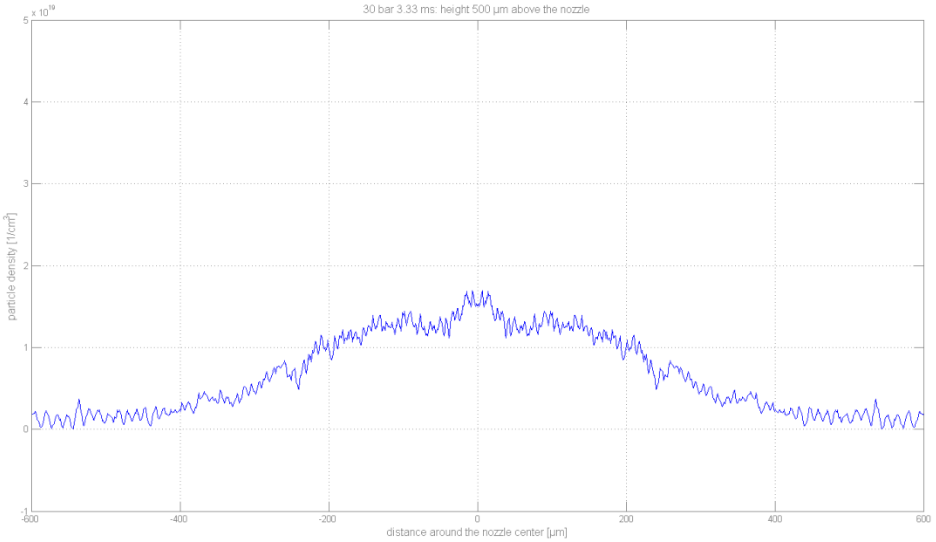

Figure 3.22: **Height scan along a horizontal axis, 500 µm above the nozzle. The particle density has a max value of 1.61 x 10^{19} particles/cm^3.**

25 bar, 3.33 ms after the trigger:

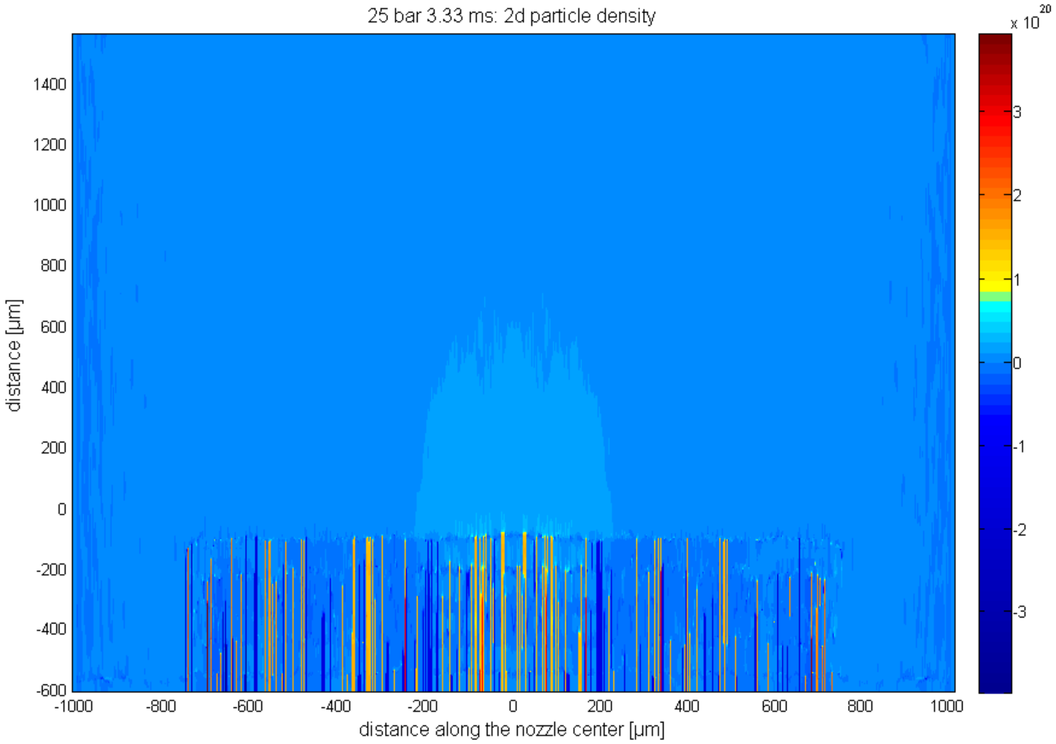

Figure 3.23: **2D particle density distribution.**

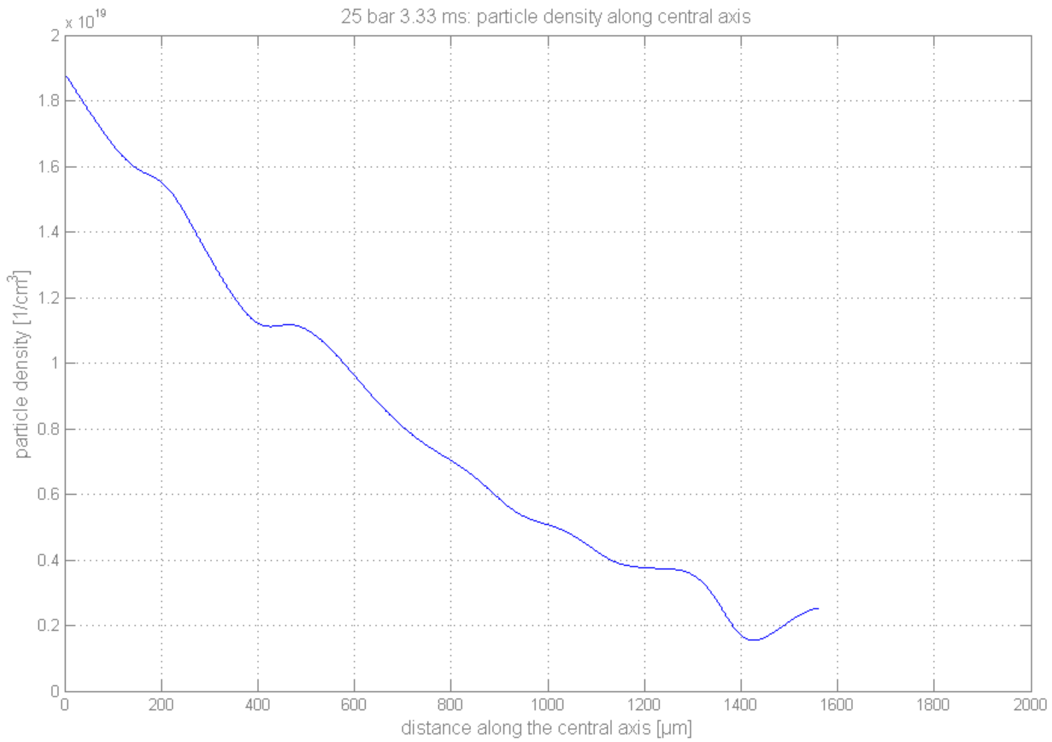

Figure 3.24: **Height scan along the vertical central axis. The particle density changes not linearly from 0 µm to 1550 µm above the nozzle edge: 1.89 x 10^{19} – 0.25 x 10^{19} particles/cm^3.**

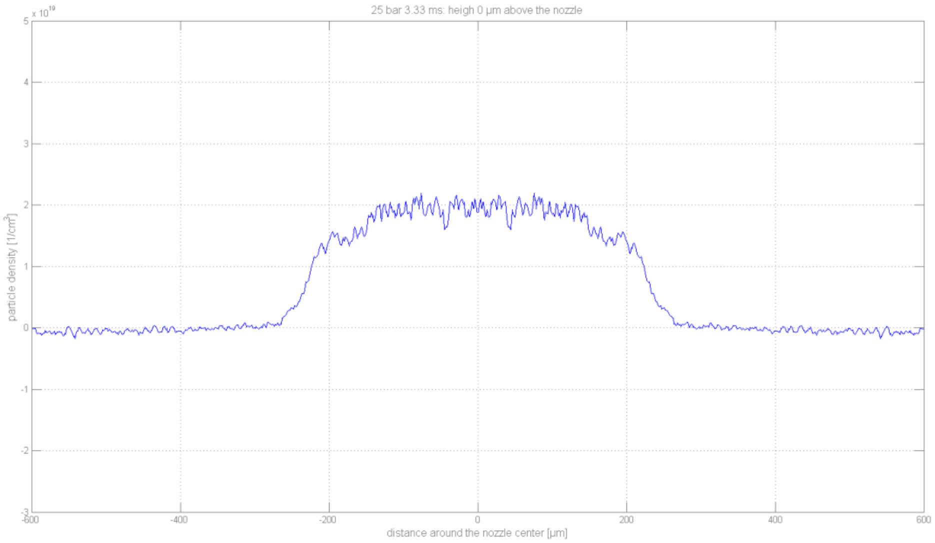

Figure 3.25: **Height scan along a horizontal axis, 0 µm above the nozzle. The particle density has a maximal value of 1.89 x 10^{19} particles/cm^3.**

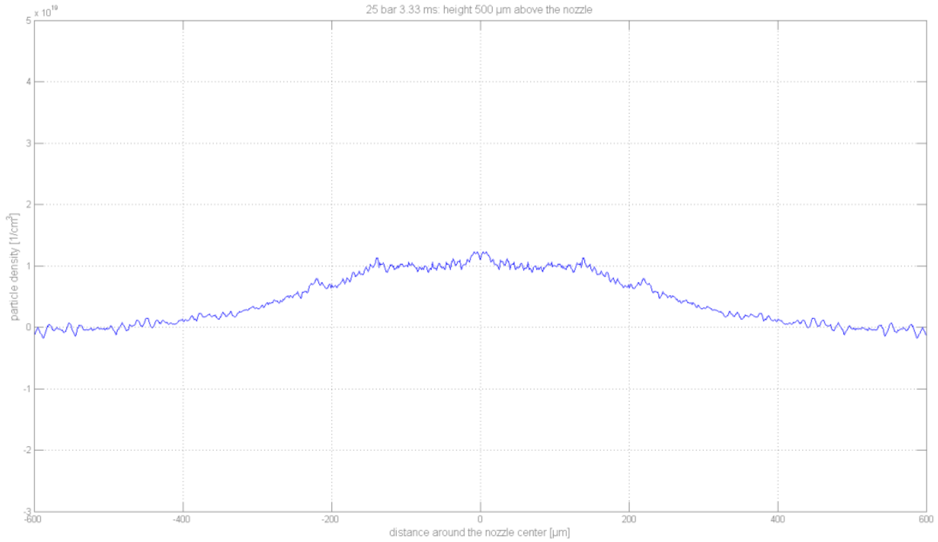

Figure 3.26: Height scan along a horizontal axis, 500 µm above the nozzle. The particle has a maximal value of density 1.1 x 10^{19} particles/cm^3.

14 bar, 3.33 ms after the trigger:

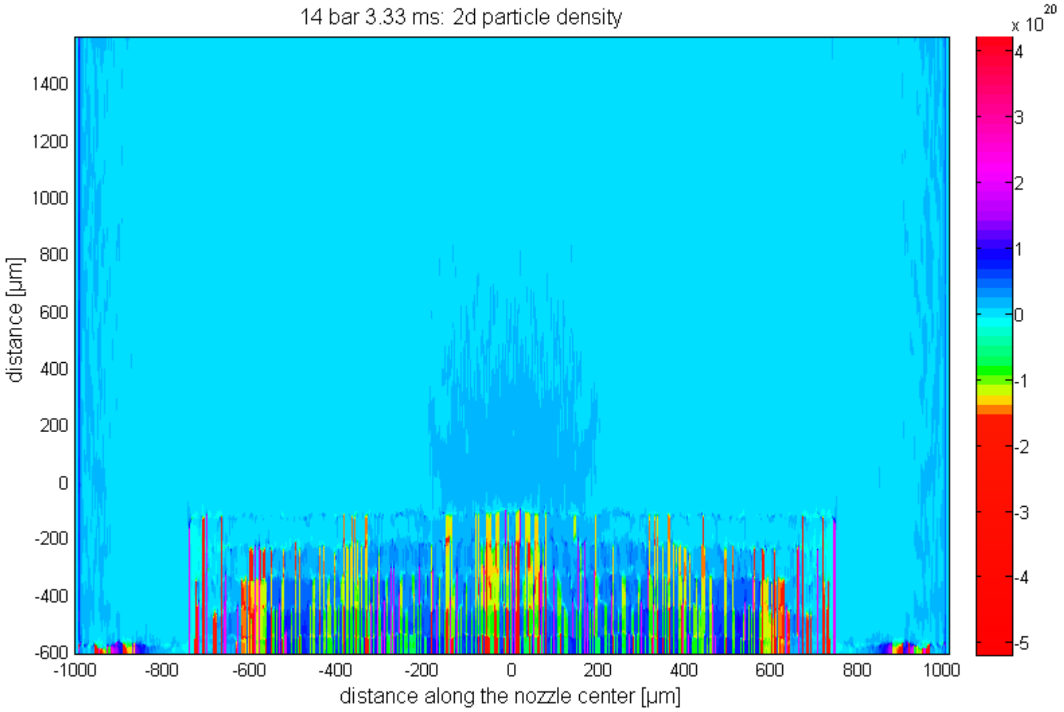

Figure 3.27: 2D particle density distribution.

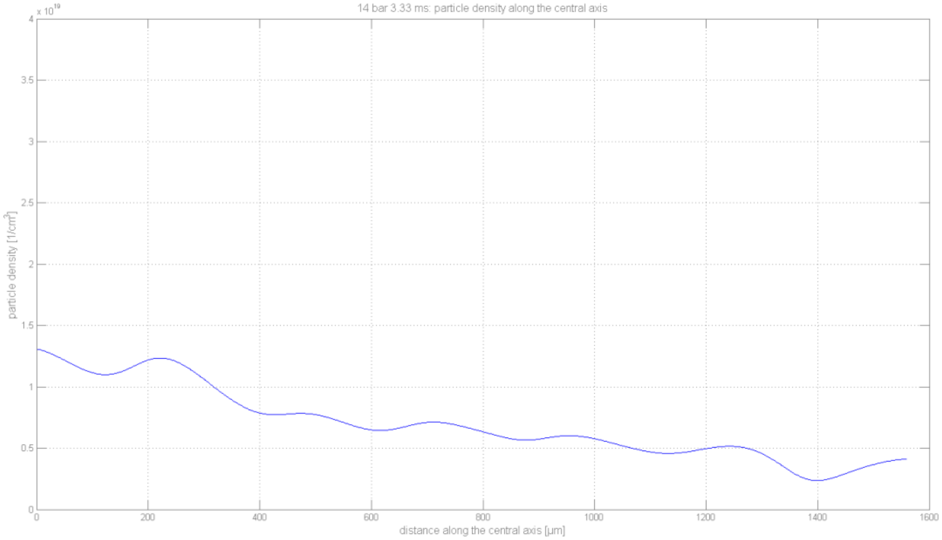

Figure 3.28: Height scan along the vertical central axis. The particle density changes not linearly from 0 µm to 1550 µm above the nozzle edge: 1.3 x 10^{19} – 0.4 x 10^{19} particles/cm^3.

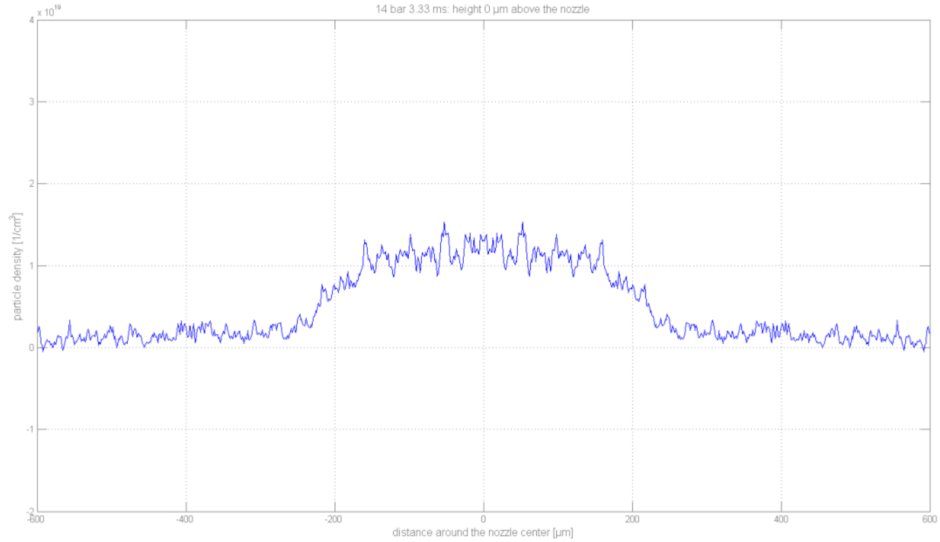

Figure 3.29: Height scan along a horizontal axis, 0 µm above the nozzle. The particle density has a maximal value of 1.3 x 10^{19} particles/cm^3.

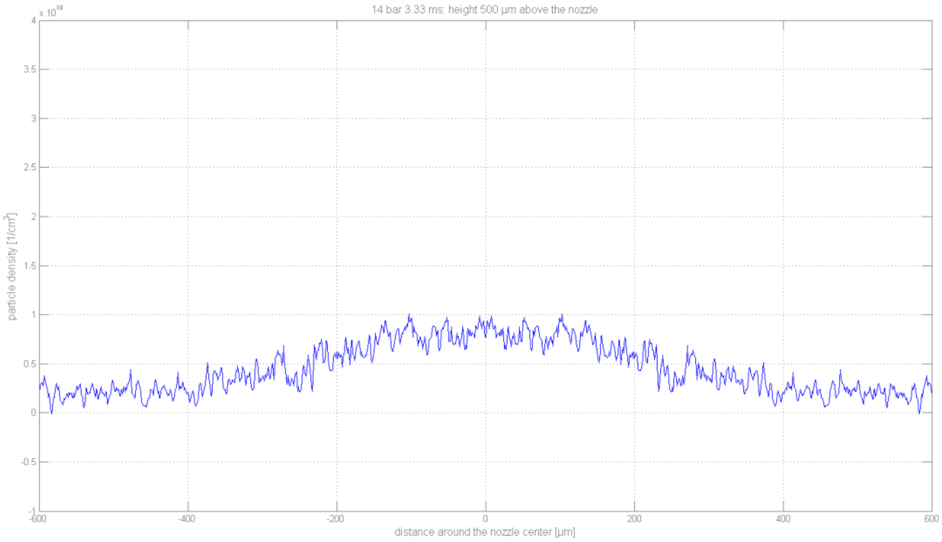

Figure 3.30: Height scan along a horizontal axis, 500 µm above the nozzle. The particle density has a maximal value of 0.9 x 10^{19} particles/cm^3.

12 bar, 3.33 ms after the trigger:

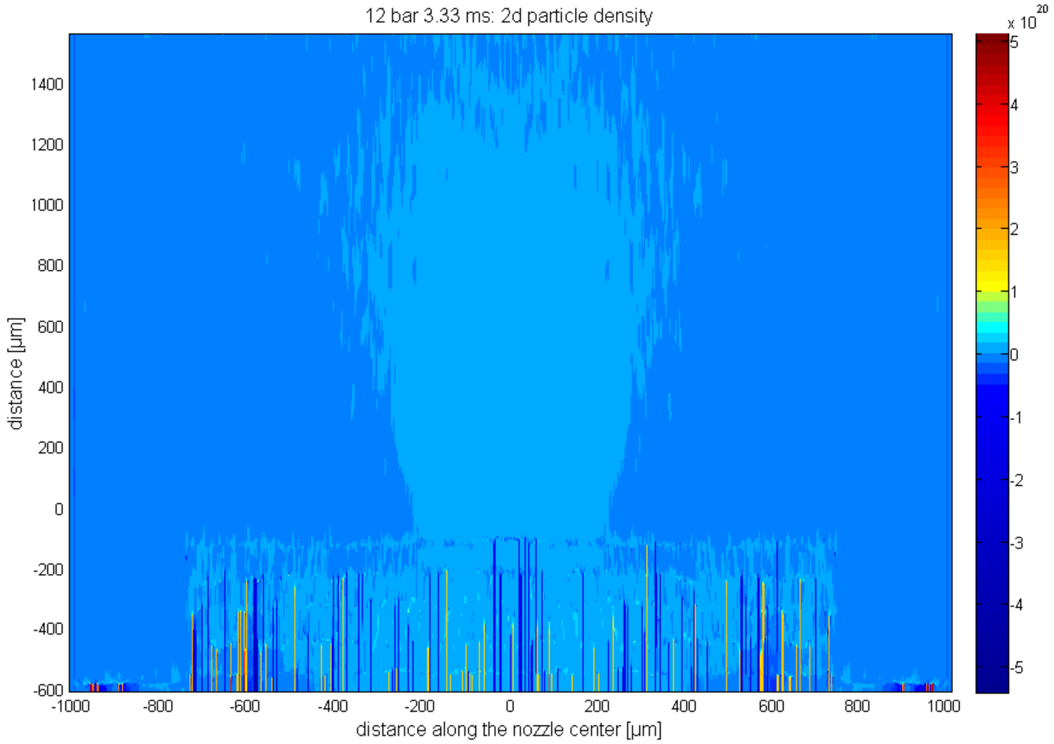

Figure 3.31: 2D particle density distribution.

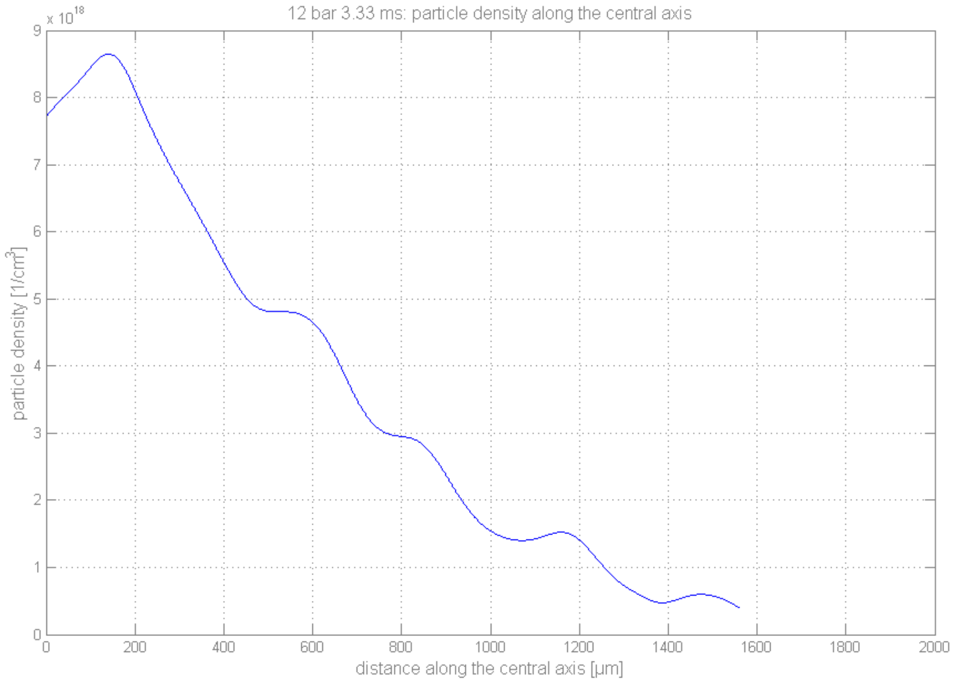

Figure 3.32: Height scan along the vertical central axis. The particle density changes not linearly from 0 µm to 1550 µm above the nozzle edge: 0.8 x 10^{19} – 0.41 x 10^{19} particles/cm^3.

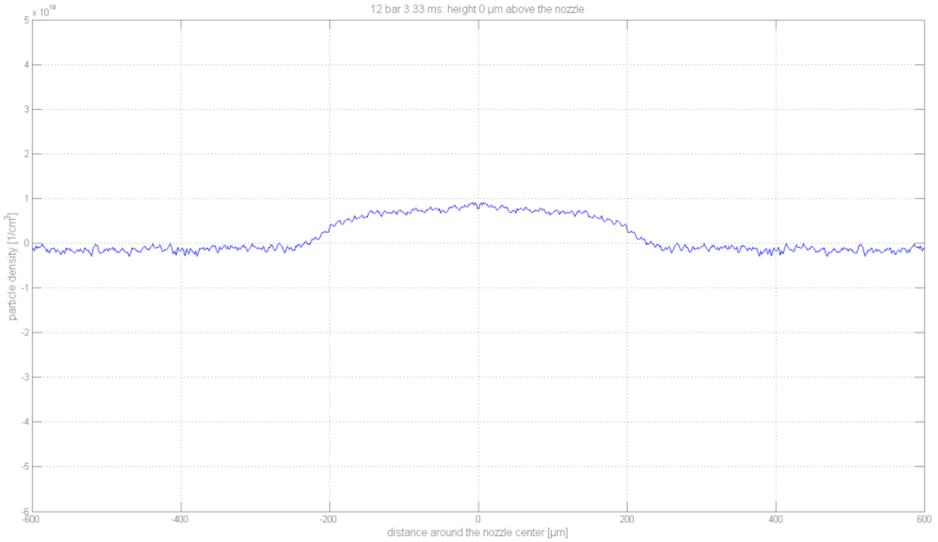

Figure 3.33: Height scan along a horizontal axis, 0 µm above the nozzle. The particle density has a maximal value of 0.8 x 10^{19} particles/cm^3.

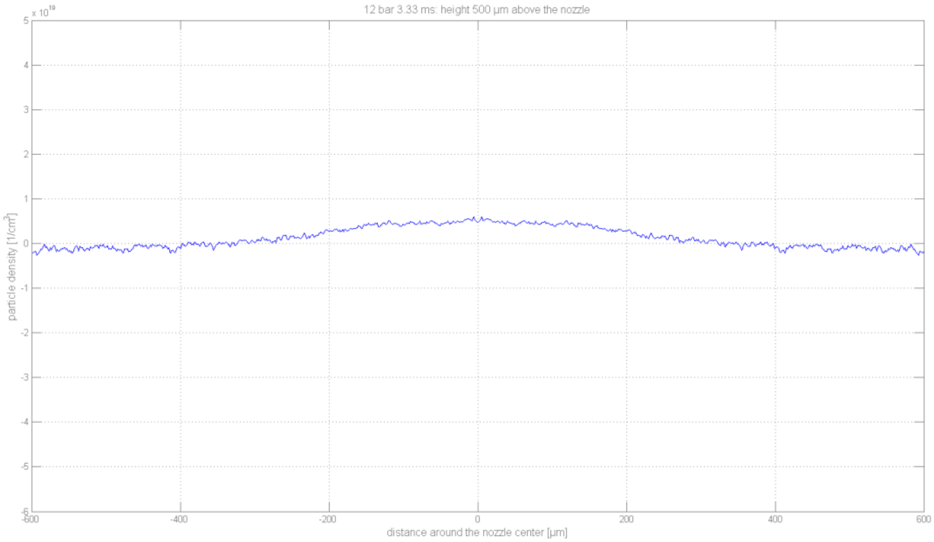

Figure 3.34: Height scan along a horizontal axis, 500 µm above the nozzle. The particle density has a maximal value of 0.51 x 10^{19} particles/cm^3.

Comparison:

The comparison of the 2d images demonstrates that each gas jet behaves in accordance with changing the argon pressure. For high pressures the difference between two shapes (*cf.* Fig. 3.11 – Fig. 3.17) are not big, but if the 2d pictures are compared for 30 and 25 bar, it is possible to see two totally different shapes of the gas jets. The gas jet for backing pressures of 30-40 bar has a long and wide shape (*cf.* Fig. 3.11, Fig. 3.17), while the gas jet for 25 bar is almost conical (*cf.* Fig. 3.21). These pictures are only illustrations of gas the jet is shapes.

According to the plots of different height scans (*e.g.* height scan along the central vertical axis and along the horizontal axes), it is possible to compare the particle density distributions for several pressures and for two height above the nozzle (*e.g.* 0 µm and 500 µm) (*cf.* Fig. 3.33).

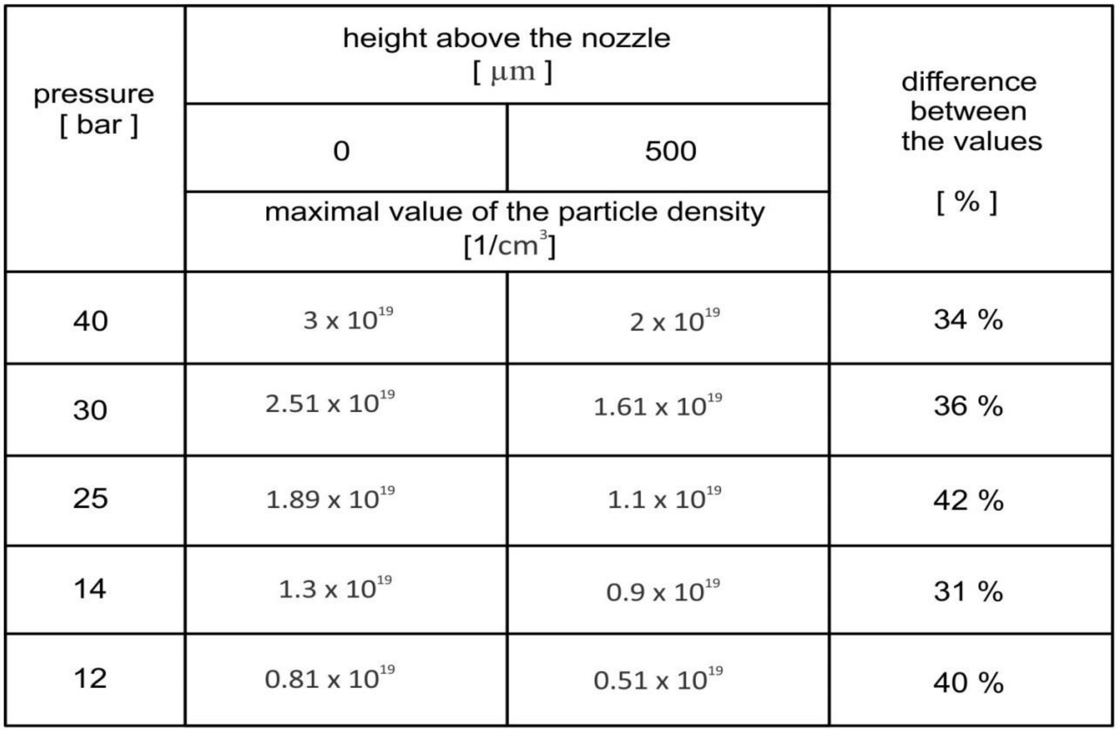

pressure [bar]	height above the nozzle [μm]		difference between the values [%]
	0	500	
	maximal value of the particle density [1/cm^3]		
40	3×10^{19}	2×10^{19}	34 %
30	2.51×10^{19}	1.61×10^{19}	36 %
25	1.89×10^{19}	1.1×10^{19}	42 %
14	1.3×10^{19}	0.9×10^{19}	31 %
12	0.81×10^{19}	0.51×10^{19}	40 %

Figure 3.35: Particle density distributions for several pressures and for heights of 0 and 500 μm.

Based on the plots for the height scans along the horizontal axes, it becomes obvious that in the high pressure cases, the particle density distribution has sharp edges for the height of 0 μm above the nozzle, while for a height of 500 μm the shapes become more plateau-like. The shapes for both heights are almost the same at low pressures.

4. Summary and Outlook

The scope of the performed experiment was to interferometrically characterize a Laval shaped nozzle with 167 µm minimal diameter. For this experiment a Mach-Zehnder interferometer was used which was built in the Central Institute for Engineering, Electronics and Analytics (ZEA-1), Forschungszentrum Jülich. The nozzle was characterized with argon at room temperature for several backing pressures and the data was analyzed by using a *Matlab* code.

The main goal of the experiment was to obtain information about the particle density distribution for the gas jet above the novel µm-nozzle. The particle density distribution was measured for two heights (0 and 500 µm above the nozzle). The data analysis showed mostly good and predicted results. Hence, it is obvious that the above mentioned µm-nozzle is useful for laser acceleration experiments.

The experiment was performed almost in ideal conditions, the experimental setup was isolated from external factors like vibrations from the turbo pump.

Of course, the setup and the measurements can be improved in some cases: One possibility is optical or mechanical additional parts *e.g.* for zooming in the images or for expanding the HeNe laser beam to larger beam diameters which would cause a better resolution of the fringes.

Another improvement can be implemented by attaching the valve on a rotation stage. Then it will be possible to take pictures from different directions aiming at a 3D characterization of the nozzle. Thus, mechanical imperfections of the nozzle geometry which can influence the shape of the particle density can be investigated easily.

Bibliography

1. WILLINGALE, L. E. A. Collimated Multi-MeV Ion Beams from High-Intensity Laser Interactions with Underdense Plasma. **Phys. Rev. Lett.**, v. 96, p. 245002, jun. 2006. ISSN 24.

2. ZEHNDER, L. Mach. L. Ein neuer Interferenzrefraktor. **Zeitschrift für Instrumentenkunde**, v. 11/12, p. 275-285/89–93, 1891/1892.

3. SCHMID, K. L. V. **Supersonic gas jets for laser-plasma experiments.** Review of Scientific Instruments, Germany , v. 83, n. 5, p. 2-4, 30 May 2012.

4. ENGIN, I. **Preparatiom for the Polarization Measurement of 3He Ions from Laser-induced plasma**. Forschungszentrum Jülich/RWTH Rheinish-Westfälische Technische Hochschule Aachen. Diploma thesis, Jülich, p. 50-52. 2011.

5. ENGIN, I. **Preparations for the Polarization Measurement of 3He Ions from Laser-induced Plasmas**. Forschungszentrum Jülich, RWTH Rheinisch-Westfälische Technische Hochschule Aachen. Diploma Thesis, Jülich, p. 7-10. 2011.

6. ENGIN, I. **Preparizations for the Polarization Measurement of 3He Ions from Laser-induced Plasmas**. Forschungszentrum Jülich, RWTH Rheinisch-Westfälische Technische Hochschule Aachen. Diploma thesis, Jülich, p. 51-53. 2011.

7. MALKA, V. **Characterization of neutral density profile in a wide range of pressure of cylindrical pulsed gas jets.** Review of Scientific Instruments, v. 71, n. 6, p. 3-5, 16 February 2000.

8. LINOS PHOTONICS GMBH & CO, K. 2. D.-3. G. **www.qioptiq-shop.com**; Data Sheet. **http:** //www.qioptiq-shop.com/out/Graphics/de/00001273_0.pdf. 2013.

9. KLEHR, F. **Private communications**. 2013.

10. PARKER Hannifin Corp. Pulse Valves Series 9-Ultra Low Leak, Extreme Performance Valve, Parker Hannifin Corp., Clevland, OH USA; Data Shet. **www.parker.com**, **http:** //www.parker.com/literature/Literature%20Files/Precision%20Fluidics%20Division/UpdatedFiles/Series9_Pulse_Valve_DataSheet.pdf>. 2013.

11. GIESEN, U. **Private communications**. 2013.

12. SPEEDCAM Mega Vis, High Speed Vision GmbH, 76131 Karlsruhe, Germany; Data Sheet. **www.hsvision.de**, **http:** //www.hsvision.de/images/stories/pdfs/flyer_MegaVis_engl.pdf. 2013.